Bidirectional control of neurovascular coupling by cortical somatostatin interneurons.

Boubacar Mohamed[1], Julie O'Reilly[1], Sandrine Picaud[1], Benjamin Le Gac[1], Esther Belzic[1], Liliana R V Castro[1], Hédi Soula[2], Isabelle Dusart[1], Dongdong Li[1], Bruno Cauli[1*]

1. Sorbonne Université, CNRS, INSERM, Neurosciences Paris Seine - Institut de Biologie Paris Seine (NPS-IBPS), 9 quai Saint Bernard, 75005 Paris, France.
2. Sorbonne Université, INSERM, Nutrition and Obesities: Systemic Approaches, NutriOmics, research unit, 91 boulevard de l'hôpital, 75013 Paris, France.

*Correspondence: bruno.cauli@upmc.fr

Keywords: Neurovascular coupling, somatostatin interneurons, nitric oxide signaling, neuropeptide Y, optogenetics

ABSTRACT

Neurovascular coupling, which links neuronal activity to cerebral blood flow, is altered early in several neurological disorders and underlies functional brain imaging. This complex process involves multiple cellular players, with inhibitory interneurons in particular receiving increasing attention, yet the mechanisms underlying how they control of cerebral blood flow remain elusive. This study elucidates the mechanisms by which somatostatin interneurons bidirectionally control neurovascular coupling. Using patch-clamp recordings in cortical slices from mouse expressing channelrhodopsin-2 in somatostatin interneurons, we observed that these neurons are supralinearly activated by low-frequency (< 5 Hz) photostimulation and are efficiently and reliably activated at frequencies up to 20 Hz. Ex vivo vascular imaging showed that low-frequency (2 Hz) photostimulation triggered vasodilation whereas high-frequency (20 Hz) photostimulation induced vasoconstriction, both dependent on action potential firing. Histochemical analysis revealed that subpopulations of cortical somatostatin interneurons expressed NOS-1, the neuronal synthesizing enzyme of the vasodilator nitric oxide, and/or the vasoconstrictor neuropeptide Y at much greater extents. Consistently, pharmacological investigations have shown that vasodilation induced by low-frequency optogenetic stimulation involves nitric oxide release and activation of its vascular receptor soluble guanylate cyclase. In contrast, the vasoconstriction induced at high-frequency photostimulation involves neuropeptide Y release and activation of the Y1 vascular receptor. These findings provide valuable insights into neurovascular coupling and help to understand the cellular mechanism underlying the functional brain imaging signals used to map brain function in both health and disease.

INTRODUCTION

Brain function and integrity are critically dependent on a permanent blood supply provided by a dense vascular network (Schaeffer and Iadecola, 2021). Cerebral blood flow (CBF) is also tightly controlled by neuronal activity, an essential process called neurovascular coupling (NVC) that is impaired in neurological disorders (Iadecola, 2017). The NVC is thought to ensure the optimal supply of metabolic needs to, and removal of waste products and heat from the activated brain regions, although its precise motive remains to be understood (Drew, 2022). It allows CBF to surge within seconds of increased neuronal activity and serves as the physiological basis for functional brain imaging techniques to map brain function (Iadecola, 2017). In the cerebral cortex, this hyperemic response is supported by dynamically controlled vasodilation that is spatially and temporally confined by vasoconstriction (Devor et al., 2007; Boorman et al., 2010; Uhlirova et al., 2016).

CBF is critically orchestrated by pial and penetrating arterioles, which have a higher density of contractile mural cells and control their diameter more rapidly than capillaries (Hill et al., 2015; Rungta et al., 2018; Hartmann et al., 2021). NVC is mediated by multiple vasoactive agents produced by excitatory neurons, astrocytes, GABAergic interneurons, and/or endothelial cells (Cauli and Hamel, 2018; Kaplan et al., 2020; Schaeffer and Iadecola, 2021) that control vessel diameter and CBF along the vascular tree (Rungta et al., 2018). These agents may be vasodilatory [e.g. arachidonic acid derivatives, nitric oxide (NO)], vasoconstrictive [e.g. Neuropeptide Y (NPY) (Uhlirova et al., 2016)], or both [e.g. glutamate, K^+ (Girouard et al., 2010; Zhang et al., 2024)].

The cellular diversity that characterizes cortical GABAergic interneurons (Ascoli et al., 2008), has made it challenging to study their contribution to NVC, and the conditions under which they release specific vasoactive agents have long remained elusive (Cauli et al., 2004). A major breakthrough in understanding their role came with the advent of transgenic mice and optogenetics, which allowed confirmation of their ability to induce vasodilation and/or vasoconstriction *in vivo* (Anenberg et al., 2015; Uhlirova et al., 2016). More recently the use of different Cre-line drivers has made it possible to investigate the contribution of different subpopulations of GABAergic interneurons (Krawchuk et al., 2019; Lee et al., 2020; Echagarruga et al., 2020; Krogsgaard et al., 2023; Ruff et al., 2024). Among these subclasses, somatostatin (Sst) interneurons have been found to either increase and/or decrease CBF

depending on the stimulation paradigm (Krawchuk et al., 2019; Lee et al., 2020), but the underlying mechanisms of this bimodal response have not been determined.

To address this unresolved issue, we used *ex vivo* approaches in combination with optogenetics to precisely control Sst interneurons firing in the mouse barrel cortex while monitoring the resulting arteriolar response. We found that Sst interneurons are supralinearly activated by low-frequency (< 5 Hz) photostimulation and are efficiently and reliably activated up to 20 Hz. Low frequency stimulation (2 Hz) induced predominantly vasodilation, whereas 20 Hz photostimulation resulted in vasoconstriction. Histochemical analyses showed that subpopulations of Sst interneurons expressed the neuronal isoform of NO synthase, NOS-1, and/or NPY at much greater extents. Pharmacological investigations revealed that both types of vascular responses were dependent on action potential (AP) firing. The vasodilation required NO synthesis and activation of the soluble guanylate cyclase (sGC), whereas the vasoconstriction involved NPY and activation of its Y1 receptor. Thus, our study elucidates the mechanisms by which Sst interneurons can induce vasodilation or vasoconstriction depending on their firing frequency.

MATERIALS AND METHODS

Animal models

Homozygous Sst-IRES-Cre mice [Jackson Laboratory, B6J.Cg-*Sst*$^{tm2.1(cre)Zjh}$/MwarJ, stock# 028864, (Taniguchi et al., 2011)] were crossed with homozygous Ai32 mice [Jackson Laboratory, B6.Cg-*Gt(ROSA)26Sor*$^{tm32(CAG-COP4*H134R/EYFP)Hze}$/J stock #024109, (Madisen et al., 2012)] or with homozygous Ai95d mice [Jackson Laboratory, B6J.Cg-*Gt(ROSA)26Sor*$^{tm95.1(CAG-GCaMP6f)Hze}$/MwarJ, stock# 028865 (Madisen et al., 2015)], to obtain heterozygous Sst$^{Cre/WT}$::Ai32$^{ChR2/WT}$ (Sst-ChR2) for optogenetic stimulations or Sst$^{Cre/Wt}$::Ai95d$^{GCaMP6f/Wt}$ (Sst-GCaMP6f) mice for immunohistochemistry. C57BL/6RJ mice were used for control optogenetic experiments and exogenous NPY applications. 16-21 days postnatal old females and males were used for all experiments. All experimental procedures involving animals were carried out in strict compliance with French regulations (Code Rural R214/87 to R214/130) and in accordance with the ethical guidelines of the Directive of the Council of the European Communities of September 22, 2010 (2010/63/EU).

87 ***Ex vivo* slice preparation**

88 Mice were deeply anesthetized by isoflurane (IsoVet Piramal Healthcare UK or IsoFlo, Axience)
89 evaporation in an induction box then euthanized by decapitation. The brain was quickly
90 removed and immersed in cold (~ 4°C) oxygenated artificial cerebrospinal fluid (aCSF)
91 containing in (mM): 125 NaCl, 2.5 KCl, 1.25 NaH_2PO_4, 2 $CaCl_2$, 1 $MgCl_2$, 26 $NaHCO_3$, 10 glucose,
92 15 sucrose and 1 kynurenic acid (Sigma-Aldrich). 300 µm-thick coronal slices containing the
93 barrel cortex were cut with a vibratome (VT1000s; Leica) and were allowed to recover at room
94 temperature for at least 45 min with oxygenated aCSF (95% O_2/5% CO_2) (Devienne et al.,
95 2018). The slices were transferred to a recording chamber and continuously perfused at a rate
96 of ~2 ml/min with oxygenated aCSF lacking kynurenic acid.

97

98 **Patch-clamp recording**

99 Borosilicate glass patch pipettes (5.0 ± 0.4 MΩ) were filled with an internal solution containing
100 (in mM): 144 K-gluconate, 3 $MgCl_2$, 0.5 EGTA, 10 HEPES, pH 7.2 (285/295 mOsm). Sst-ChR2
101 interneurons were first visually identified by their EYFP fluorescence. Whole-cell recordings
102 were performed at room temperature (20-25 °C) using a patch clamp amplifier (Axopatch
103 200B, Molecular Devices) at a wavelength of 780 nm, which does not activate ChR2 (Lin et al.,
104 2009). Data were filtered at 5-10 kHz and digitized at 50 kHz using an acquisition board
105 (Digidata 1440, MDS) attached to a personal computer running pCLAMP 10.7 software
106 package (MDS). Electrophysiological properties were determined using the fast I-clamp mode
107 of the amplifier and were measured as previously described (Karagiannis et al., 2021, 2009).
108 Membrane potential values were not corrected for liquid junction potential. Only neurons
109 with a resting membrane potential more hyperpolarized than -55 mV were further analyzed.

110

111 **Optogenetic stimulation**

112 Optogenetic stimulation performed through the objective using a 470 nm light-emitting diode
113 (LED) device (CoolLED brand, Precise Excite model) attached to the epifluorescence port of a
114 BX51WI microscope (Olympus) and a set of multiband filters consisting of an excitation filter
115 (HC 392/474/554/635, Semrock), a dichroic mirror (BS 409/493/573/652, Semrock), and an
116 emission filter (HC 432/515/595/730, Semrock). Photostimulation consisted of a 10-s train of
117 5 ms light pulses at an intensity of 38 mW/mm² and delivered at six different frequencies (1,
118 2, 5, 10, 20 and 40 Hz).

119 **Vascular imaging**

120 Blood vessels and cells were observed in slices under infrared illumination with Dodt gradient
121 contrast optics (IR-DGC Luigs and Neumann; (Dodt and Zieglgansberger, 1998)) using a
122 collimated LED (780 nm; ThorLabs) as the transmitted light source, a 40X (LUMPlanF/IR,
123 40X/0.80 W, Olympus) and a digital camera (OrcaFlash 4.0LT+, Hamamatsu) attached to the
124 microscope. Diving arterioles were selected by IR-DGC based on their well-defined luminal
125 diameter (16.7 ± 0.5 µm, n = 144 arterioles), their length remaining in the focal plane of at
126 least 50 µm, and the thickness of their wall (5.5 ± 0.1 µm, n = 144 arterioles). A resting period
127 of at least 30 min (Lovick et al., 1999; Zonta et al., 2003) was observed after slice transfer. IR-
128 DGC images were acquired at 0.1 Hz for pharmacological applications and at 1 Hz for
129 optogenetic experiments using Imaging Workbench 6.1 software (Indec Biosystems). The focal
130 plane was continuously maintained on-line using IR-DGC images of cells as anatomical
131 landmark (Lacroix et al., 2015). After light-induced responses, arteriolar identity and reactivity
132 were systematically verified by assessing their contractility (Hartmann et al., 2021) using the
133 thromboxane A2 analog, U46619 (100 nM) (Cauli et al., 2004; Rancillac et al., 2006). Blood
134 vessels that failed to constrict after this pharmacological application were discarded. Only one
135 arteriole was monitored per slice.

136

137 **Double fluorescence immunolabeling**

138 Mice were euthanized with Pentobarbital (150 mg/kg, i.p., Euthasol Vet) and their brain were
139 perfusion-fixed (50 ml of ice-cold 4 % paraformaldehyde (PFA), in 0.1M phosphate buffer, pH
140 7.4), and post-fixed by immersion in 4 % PFA (2 h, 4°C). Brains were then cut in 50 µm-thick
141 coronal sections with a VT-1000S vibratome (Leica). After washing in PBS, free-floating
142 sections were blocked for 2 h at room temperature in a PBS 1X/0.25% Triton X-100/0,2%
143 gelatin solution before being incubated overnight at 4°C with primary antibodies. Sections
144 from 3 to 4 different mouse brains were simultaneously incubated overnight with the primary
145 antibodies against GFP and specific markers. Antibodies included chicken anti-GFP (1:1000;
146 Aves Labs GFP-1020, (Tricoire et al., 2010)), rabbit anti-NOS-1 (1:1000, Millipore AB5380,
147 (Tricoire et al., 2010)), sheep anti-NPY (1:2000, Abcam ab6173, (Lee et al., 2010)). The
148 respective immunoreactions were visualized with the following secondary antibodies: goat
149 anti-chicken Alexafluor 488 (1:1000, Invitrogen A11039), donkey anti-rabbit Alexafluor 555
150 (1:1000, Invitrogen A31572) donkey anti-sheep Alexafluor 555 (1:1000, Invitrogen A21436).

151 Nuclear counterstaining was performed with 100 ng/ml DAPI (4',6-diamidino-2-phenylindole;
152 Invitrogen) solution in PBS for 20 min. Sections were mounted with Fluoromount G
153 (SouthernBiotech) on gelatin-coated slides for visualization. Images of immunostained
154 material were acquired and processed in Airyscan 2 mode using a LSM 980 confocal
155 microscope with a 20x objective (N Plan-Apochromat 20x) and ZEN Blue 3 software (Zeiss).
156 Cell counting was achieved using the cell counter plug-in of FIJI software.
157
158 **Drugs**
159 All pharmacological compounds were bath-applied after a 5-minute control period (aCSF) and
160 vascular dynamics were recorded during bath application. The following drugs were dissolved
161 in water: NPY (Enzo, ALX-163-003), Nω-Nitro-L-arginine methyl ester hydrochloride (L-NAME,
162 Sigma-Aldrich, N5751), BIBP3226 (1 µM, Tocris, 2707). Tetrodotoxin (TTX, 1 µM, Latoxan,
163 L8503) was dissolved in 90% acetic acid. 1H-[1,2,4] oxadiazolo[4,3-a]quinoxalin-1-one (ODQ,
164 Sigma-Aldrich, O3636) was dissolved in DMSO and 9,11-dideoxy-9α,11α-methanoepoxy
165 prostaglandin F2α (U-46619, 100 nM, Enzo, BML-PG023) in ethanol. Acetic acid, DMSO and
166 ethanol doses were always used below 0.1% to avoid vascular interactions (Sun et al., 2010).
167 NO pathway inhibitors, BIBP3226 and TTX were applied at least 30 min before optogenetic
168 stimulation or exogenous NPY application.
169
170 **Vascular reactivity analysis**
171 To compensate for potential x-y drifts, all images were realigned off-line using the "StackReg"
172 plug-in (Thevenaz et al., 1998) of the ImageJ 1.54f software. Luminal diameter was measured
173 on registered images using custom analysis software developed in MATLAB (MathWorks)
174 (Lacroix et al., 2015). Only arterioles with a stable luminal diameter were analyzed further.
175 Arterioles were considered stable if the relative standard deviation (RSD) of their luminal
176 diameter during the baseline period was less than 5% (Lacroix et al., 2015). The impact of
177 blockers, inhibitors, and antagonists on arterioles was evaluated by comparing the mean
178 luminal diameter during the initial 5 minutes of the baseline period and the final 5 minutes of
179 the treatment period prior to optogenetic stimulation or NPY application. Diameter changes
180 ($\Delta D/D_0$) were expressed according to: $(Dt - D_0)/D_0$ where Dt is the luminal diameter at the
181 time t and D_0 the average diameter during the 5 minutes baseline period. Vasomotor
182 responses and their parameters were determined from the diameter change traces [$\Delta D/D_0$ =

183 f(t)] plotted using Clampfit 10.7 (MDS). To determine whether arterioles dilated or
184 constricted, a Z-score was calculated from the diameter change traces using the formula: $Z =$
185 $(x - \mu)/ \sigma$, where both the mean μ and standard deviation σ were calculated using the values
186 before photostimulation or NPY application. Vascular responses were classified as
187 vasodilation or vasoconstriction, respectively, if the Z-score exceeded a value of 1.96 (95%
188 criteria) or fell below -1.96 for 10 seconds and 1 minute for photostimulation and NPY
189 application, respectively. For each vascular response, the time of onset and peak (relative to
190 the beginning of stimulation), duration, maximal amplitude and magnitude (area under the
191 curve [AUC]) were determined (Supplementary Fig. 2). When multiple events of vasodilation
192 or vasoconstriction occurred, the earliest onset was used for global onset, the time and
193 amplitude of the largest maximum amplitude were used for global time to peak and global
194 maximum amplitude, and the sum of durations and magnitudes was used for global duration
195 and magnitude.
196
197 **Statistical analyses**
198 Statistical analyses were performed using GraphPad Prism version 8.0.2 (GraphPad Software,
199 La Jolla, California, USA). All values are expressed as means ± SEM. Normality of distribution
200 was assessed using the Shapiro-Wilk test. Parametric tests were only used if this criterion was
201 met. The mean spike success rate per light pulse between photostimulation frequencies was
202 compared using the Q Friedman test. Comparisons of vascular responses were determined
203 using Brown-Forsythe ANOVA or Kruskal-Wallis tests. Given p-values were corrected for
204 multiple comparisons using the original False Discovery Rate method of Benjamini and
205 Hochberg (Benjamini and Hochberg, 1995). Statistical significance on all figures uses the
206 following convention: $*p < 0.05$, $**p < 0.01$ and $***p < 0.001$.
207

208 **RESULTS**

209 **Sst interneurons are efficiently activated by optogenetic stimulation over a wide range of**
210 **frequencies.**

211 To evaluate the frequency dependence of the vascular response driven by Sst interneurons,
212 we optogenetically elicited their AP firing while visualizing the evoked vascular response in
213 cortical brain slices from $Sst^{Cre/WT}$::$Ai32^{ChR2/WT}$ mice (Madisen et al., 2012; Taniguchi et al.,
214 2011) conditionally expressing the H134R variant of channelrhodopsin-2 (ChR2) in Sst
215 interneurons. We first determined the electrophysiological phenotype of Sst-ChR2 cortical
216 neurons using whole-cell patch clamp recordings. Cortical neurons expressing EYFP/ChR2
217 were selected based on their EYFP fluorescence (Fig. 1a and Supplementary Fig. 1) in layers II-
218 III (n=13 neurons) and V (n=3 neurons). Most neurons exhibited electrophysiological features
219 typical of adapting-Sst interneurons (Karagiannis et al., 2009, 2021; Perrenoud et al., 2012a),
220 including a relatively high membrane resistance (608 ± 231 MΩ) and a pronounced voltage
221 sag (21.2 ± 10.8 %) in response to hyperpolarizing current pulses (Fig. 1a, middle traces). They
222 also exhibited a low rheobasic current (8 ± 14 pA, Fig. 1a) and a slowly developing early
223 frequency adaptation (adaptation time constant: 60.5 ± 23.8 ms) when depolarized by high
224 stimulation intensities (Fig. 1a). Consistently, the hyperpolarization (AHP) phase of their action
225 potentials consisted of a fast AHP, followed by an afterdepolarization (ADP) and a medium
226 AHP (Fig. 1a and Supplementary Table 1). However, as previously reported in Sst-Cre cortical
227 neurons (Hu et al., 2013) and expected from the occasional expression of Sst transcripts in
228 parvalbumin neurons (Cauli et al., 1997; Tasic et al., 2016), one Sst-ChR2 neuron exhibited the
229 electrophysiological features of a fast spiking cell with a low input resistance (129 MΩ), a fast
230 time constant (11.7 ms), a high rheobase (185 pA), short spikes (0.6 ms) with a sharp fast AHP
231 (-26.5 mV), and the ability to fire high firing rates (maximal frequency: 99 Hz) with little
232 frequency adaptation (Supplementary Fig. 1 and Table 1).

233 Next, we evaluated the efficiency of optogenetic stimulation by recording the voltage
234 response of the patched Sst-ChR2 neurons. Wide-field photostimulation was achieved using
235 10-second trains of 5 ms light pulses (see Materials and Methods) delivered at six different
236 frequencies (1, 2, 5, 10, 20 and 40 Hz, Fig. 1b, lower traces). Surprisingly, at the beginning of
237 the light pulse trains, Sst-ChR2 neurons fired up to five APs per light pulse (Fig. 1b, upper
238 traces). Such bursting response declined within seconds before reaching a steady state level
239 (Fig. 1b, middle traces). The instantaneous spike success rate remained above 100 % at

240 stimulation frequencies below 10 Hz, while it decreased below 100% at higher frequencies
241 (Fig. 1b, middle traces). Consistent with the kinetic properties of the H134R ChR2 variant (Lin
242 et al., 2009), Sst-ChR2 neurons were not able to sustain the firing of action potentials when
243 photostimulated at 40 Hz (Fig. 1b6). The mean spike success rate over the 10 s train differed
244 between photostimulation frequencies (Fig. 1c, $Q_{(6,9)}$= 41.89, p= 6.203 10^{-8}, 1 Hz: 176 ± 13%;
245 2 Hz: 197 ± 15%; 5 Hz: 118 ± 11%; 10 Hz: 103 ± 10%; 20 Hz: 97 ± 5%; 40 Hz: 25 ± 7%, n=9 Sst-
246 ChR2 neurons). Indeed, photostimulation at 1 Hz and 2 Hz showed a higher number of APs per
247 light pulse than that observed at frequencies above 5 Hz (Fig. 1c, 1Hz vs. 10 Hz, p= 0.0374; 1Hz
248 vs. 20 Hz, p= 0.0063; 1 Hz vs. 40 Hz, p= 7.000 10^{-6}; 2 Hz vs. 10 Hz, p = 0.0245; 2Hz vs. 20 Hz, p=
249 0.0039, 2 Hz vs. 40 Hz, p=3.597 10^{-6}). Taken together, these observations indicate that
250 optogenetic stimulation efficiently and reliably activates Sst-ChR2 neurons, mostly of the
251 adapting Sst subtype, at frequencies up to 20 Hz. They also reveal that these neurons over-
252 respond to low frequencies of photostimulation.
253
254 **The polarity of the vascular response induced by the optogenetic stimulation of Sst-ChR2**
255 **neurons is frequency dependent.**
256 Next, we visualized the optogenetically induced response of diving arterioles in cortical slices
257 (Fig. 2). We focused on the photostimulations at 2 Hz and 20 Hz, which correspond
258 respectively to the highest AP number per light pulse and to the frequency that produced the
259 highest total AP number, respectively (Fig. 1b,c). When photostimulation was delivered at 2
260 Hz in Sst-ChR2 slices, we observed that the vast majority of arterioles exhibited vasodilatory
261 events (n= 13 of 14 arterioles, Fig. 2a,b), which could be accompanied by vasoconstrictive
262 events (n=6 of 14). On average, this resulted in a slight vasodilation (Fig. 2c). High light
263 intensity can cause dilation (Rungta et al., 2017) or constriction (Choi et al., 2010) independent
264 of ChR2, so we did control experiments by repeating 2 Hz photostimulation in slices of C57Bl6
265 mice that do not express ChR2 (Fig. 2c). Although the overall vascular response, as estimated
266 by the area under the curve (AUC) of the response following the optogenetic stimulation did
267 not differ between Sst-ChR2 (55.8 ± 24.1 %.min, n= 14 arterioles) and C57Bl6 arterioles (37.4
268 ± 15.3 %.min, n= 6 arterioles, p= 0.15146, Fig. 2g1), an evident tendency was observed toward
269 vasodilation in Sst-ChR2 arterioles (Fig. 2c). Because both vasodilation and vasoconstriction
270 can occur in the same arteriole (Fig. 2b), we refined the analysis of vascular responses by
271 separating vasodilatory events from vasoconstrictive events based on a Z-score test

272 (supplementary Fig. 2a-b, see Methods). The magnitude of vasodilation was greater in Sst-
273 ChR2 arterioles (69.6 ± 19.9 %.min, Fig. 2g2) than in control arterioles (8.5 ± 4.5 %.min,
274 p=0.03415), although not the maximal amplitude (Sst-ChR2: 6.1 ± 1.3 % *vs.* C57Bl6: 2.2 ± 0.7
275 %, p= 0.12763, Fig. 2g3). Vasodilation also occurred earlier and lasted longer in Sst-ChR2
276 arterioles (onset: 221 ± 130 s, duration: 1121 ± 195 s) than in control arterioles (onset: 1013
277 ± 314 s, p= 0.02501, Fig. 2g4, duration: 304 ± 135 s, p= 0.04865, Fig. 2g6) but did not differ in
278 their time to peak (Sst-ChR2: 669 ± 155 s *vs.* C57Bl6: 1014 ± 314 s, p= 0.32174, Fig. 2g5). In
279 contrast, the amplitude, magnitude, and kinetic properties of vasoconstriction induced by
280 photostimulation at 2 Hz did not differ between Sst-ChR2 and C57Bl6 arterioles
281 (supplementary Fig. 2c1-5).
282 We next evaluated whether a stronger optogenetic stimulation could induce a similar vascular
283 response. Surprisingly, photostimulation at 20 Hz of Sst-ChR2 slices (n= 16) induced
284 vasoconstrictive events in the vast majority of arterioles (n= 15 of 16), but also vasodilatory
285 events to a lesser extent (n=9 of 16, Fig. 2d,e). This resulted on average in a progressive
286 vasoconstriction that was not observed in control arterioles (n= 4, Fig. 2f). Although the overall
287 vascular response was not statistically different between Sst-ChR2 and C57Bl6 arterioles
288 (p=0.13458, Fig. 2h1), similarly to 2 Hz photostimulation it was more heterogeneous in Sst-
289 ChR2 arterioles (-83.3 ± 46.7 %.min) than in C57Bl6 arterioles (0.0 ± 25.3 %.min) and may be
290 associated with both vasoconstriction and vasodilation (Fig. 2d,e and supplemental Fig. 2 a,b).
291 Both the magnitude of vasoconstriction and the maximal vasoconstriction were greater in Sst-
292 ChR2 arterioles (AUC: -121.7 ± 35.4 %.min, Fig. 2h2; Maximal constriction: -12.2 ± 2.7 %, Fig.
293 2h3) than in control C57Bl6 (AUC: -17.8 ± 17.8 %.min, p=0.01810; Maximal constriction: -1.6
294 ± 1.6 %, p=0.00505). The onset and time to peak of vasoconstriction were also earlier in Sst-
295 ChR2 arterioles (onset: 267 ± 120 s, Fig. 2h4; time to peak: 874 ± 181 s, Fig. 2h5) compared to
296 control C57Bl6 arterioles (onset: 1361 ± 439 s; p= 0.01993; time to peak: 1680 ± 121 s, p=
297 0.04397). The contraction duration did not differ between Sst-ChR2 arterioles (981 ± 152 s)
298 and C57Bl6 (424 ± 424 s, p= 0.13849, Fig. 2h6). In contrast, the amplitude, magnitude, and
299 kinetic properties of vasodilatory events induced by photostimulation at 20 Hz did not differ
300 between Sst-ChR2 and C57Bl6 arterioles (supplementary Fig. 2d1-5). Taken together, these
301 observations indicate that, depending on the frequency of optogenetic stimulation Sst-ChR2
302 neurons elicit a bidirectional vascular response consisting mainly of vasodilation and
303 vasoconstriction at 2 Hz and at 20 Hz, respectively.

304

305 **NOS-1 and NPY are expressed by subpopulations of Sst cortical interneurons**

306 Subpopulation of Sst-expressing cortical interneurons have been reported to produce NO
307 and/or NPY (Hendry et al., 1984; Kubota et al., 1994, 2011; Perrenoud et al., 2012a). These
308 mediators may explain the bidirectional vascular responses induced by the photostimulation
309 of Sst-ChR2 interneurons at 2 and 20 Hz, respectively, as they have been shown to induce
310 vasodilation and vasoconstriction, respectively (Cauli et al., 2004; Rancillac et al., 2006). We
311 therefore used double immunohistofluorescence to determine the extent to which Sst
312 interneurons have the ability to produce NO and NPY. Consistent with previous reports
313 (Kubota et al., 1994, 2011; Perrenoud et al., 2012a), NOS-1 immunolabeling revealed that
314 strongly immunoreactive somata appeared denser in deep than in superficial cortical layers
315 (Fig. 3a2-3 and supplementary Fig. 3). Some of these neurons were clearly identified as Sst-
316 ChR2 interneurons as shown by immunolabelling of the ChR2-EYFP fusion transgene using an
317 anti-GFP antibody (supplementary Fig. 3). However, consistent with the membrane
318 localization of ChR2-EYFP (Fig. 1a and supplementary Fig. 1), GFP immunofluorescence was
319 present at the periphery of the somata and in a dense fiber plexus (supplementary Fig. 3)
320 making it difficult to evaluate the degree of co-expression. Therefore, we thus used Sst-
321 GCamp6 mice (n= 3 mice) to obtain somatic Cre-dependent expression of the circularly
322 permuted GFP of GCamp6 (Madisen et al., 2015). As previously reported in Sst-IRES-Cre mice
323 (Taniguchi et al., 2011), Cre-dependent GFP expression was observed in the somata of neurons
324 distributed throughout all cortical layers except layer I (Fig. 3a1,b1), which nevertheless
325 showed diffuse GFP labelling presumably originating from the ascending axon of Martinotti
326 cells branching in this layer (DeFelipe et al., 2013). The average density of GFP-positive cells
327 was comparable between sections immunostained for NOS-1 (49.9 ± 2.7 cells/mm^2, n=3 mice,
328 Fig. 3a1) and NPY (41.0 ± 7.1 cells/mm^2, n= 3 mice, Fig. 3b1, t(2.55619)= 1.16763, p= 0.3403).
329 A similar density of neurons immunolabeled for NOS-1 was observed in GFP positive (2.0 ± 0.1
330 cells/mm^2) and negative cells (1.9 ± 0.4 cells/mm^2, t(2.28582)= 0.215387, p= 0.8472, Fig. 3a3-
331 4). However, the intensity of NOS-1 immunostaining was stronger in GFP-positive cells than in
332 negative cells (Fig. 3a1,2), indicating that they likely correspond to type 1 and type 2 NO-
333 producing interneurons, respectively. Consistent with previous reports in Sst interneurons,
334 (Kubota et al., 1994, 2011; Karagiannis et al., 2009; Perrenoud et al., 2012a; Tricoire et al.,
335 2013), putative type 1 NO interneurons represented only a minority of GFP-positive cells (4.0

336 ± 0.1%). NPY immunostaining showed a relatively high density of positive cells (29.4 ± 6.0
337 cells/mm^2) and fiber plexus in superficial and deep layers (Fig. 3b2) as reported in other
338 mammals (Hendry et al., 1984). The vast majority of NPY immunoreactive neurons were also
339 GFP positive (81.4 ± 2.1%, Fig. 3b3-4) with the remaining NPY interneurons likely
340 corresponding to neurogliaform cells (Cauli et al., 2004; Price et al., 2005; Karagiannis et al.,
341 2009; Kubota et al., 2011; Perrenoud et al., 2012a), as suggested by their round
342 immunolabeled somata (Fig. 3b3-4). More precisely, the proportion of GFP-positive cells
343 immunostained for NPY was much higher (58.9 + 8.2%, t(2.00020)=6.70695, p= 0.0215) than
344 those immunolabeled for NOS-1, which is known to represent a subpopulation of NPY
345 interneurons (Estrada and DeFelipe, 1998; Karagiannis et al., 2009; Tasic et al., 2016). These
346 observations collectively indicate that the Cre-dependent expression of the transgenes in Sst-
347 IRES-Cre mice occurs in at least two subpopulations of interneurons that express NOS-1
348 and/or NPY to a greater extent.
349
350 **Vasodilation induced by 2 Hz photostimulation of Sst-ChR2 interneurons requires AP firing**
351 **and NO signaling**
352 Since a subpopulation of Sst interneurons (Fig. 3a3-4 and supplementary 3) can produce the
353 vasodilator NO (Cauli et al., 2004), we next investigated the mechanisms by which they induce
354 vasodilation when photostimulated at 2 Hz. We first determined whether spiking activity was
355 required by blocking APs with the voltage-activated sodium channel blocker tetrodotoxin (TTX
356 1 µM (Zonta et al., 2003), n= 10 arterioles). Bath application of TTX did not change arteriolar
357 diameter (diameter before: 17.0 ± 1.8 µm *vs.* after TTX: 16.9 ± 1.7 µm, $t_{(9)}$= 1.0031, p=0.3420,
358 Supplementary Fig. 4a,b), indicating that basal network activity does not influence the resting
359 vascular tone. By contrast, it dramatically reduced the overall vascular response (-19.6 ± 10.5
360 %.min, p= 0.04966, Fig. 4a and d1) and the magnitude of evoked vasodilation (6.8 ± 2.4 %.min,
361 p= 0.00844, Fig. 4d2) without altering the maximal dilation (2.2 ± 0.6%, p=0.11114, Fig. 4d3)
362 or its time to peak (1256 ± 192 s, p= 0.07716, Fig. 4e2). In addition, the onset and the duration
363 of vasodilation were respectively delayed (1142 ± 210 s, p= 0.00152, Fig. 4e1) and shortened
364 (306 ± 121 s, p= 0.01623, Fig. 4e3). Of note, the vasoconstrictive events were not altered
365 except for their onset and time to peak (Supplementary Fig. 4g1-5). These observations
366 indicate that AP firing is mandatory for the vasodilation induced by 2 Hz photostimulation.

367 We next asked whether NO signaling could be responsible for the vasodilation induced by 2
368 Hz photostimulation. Inhibiting nitric oxide synthases with L-NAME (100 µM (Zonta et al.,
369 2003), n = 9 arterioles) did not alter the arteriolar diameter (diameter before: 15.3 ± 2.1 µm
370 *vs.* after L-NAME: 15.4 ± 2.3 µm, $W_{(9)}$= -2, p=0.9453, Supplementary Fig. 4c,d) indicating that
371 basal NO synthase activity does not influence resting vascular tone. By contrast L-NAME
372 treatment completely abolished the evoked vasodilation as evidenced by its dramatic impact
373 on the overall vascular response (AUC: -71.0 ± 20.4 %.min, p= 0.00042, Fig. 4b and 4d1), as
374 well as on the magnitude (4.9 ± 2.9 %.min, p = 0.00096, Fig. 4d2) and maximal amplitude of
375 vasodilation (1.5 ± 0.9%, p= 0.00172, Fig. 4d3). It also strongly delayed the apparent onset of
376 vasodilation (1407 ± 210 s, p= 0.0004, Fig. 4e1) and reduced its duration (169 ± 100 s,
377 p=0.00059, Fig. 4e3), but not the time to peak (1410 ± 210 s, $H_{(4,54)}$= 8.299, p= 0.08123, Fig.
378 4e2). The overall negative responses observed under NOS inhibition suggest that
379 vasoconstriction was uncovered. Indeed, L-NAME increased the magnitude (-70.1 ± 19.7
380 %.min, p= 0.00234, Supplementary Fig. 4g1) and the maximal amplitude (-8.6 ± 1.9 %, p=
381 0.00089, Supplementary Fig. 4g2) of vasoconstrictive events induced by 2 Hz
382 photostimulation. It also shortened their onset (475 ± 207s, p= 0.01292, Supplementary Fig.
383 4g3) without affecting their time to peak (1056 ± 185 s, p= 0.06502, Supplementary Fig. 4g4)
384 and duration (926 ± 155 s, $H_{(4,54)}$=9.278, p= 0.05452, Supplementary Fig. 4g5). These
385 observations suggest that the vasodilation evoked by 2 Hz photostimulation involves NO
386 synthesis, and that its blockade unmasks vasoconstriction. To confirm that NO signaling is
387 required, we next used ODQ (10 µM (Hepp et al., 2007), n= 12 arterioles) to inhibit the sGC,
388 the intracellular receptor responsible for NO-mediated vasodilation. Similar to NOS inhibition,
389 blockade of NO-signaling did not alter the basal diameter (diameter before: 19.3 ± 2.9 µm *vs.*
390 after ODQ: 19.2 ± 2.9 µm, $W_{(12)}$= -14, p=0.6055, Supplementary Fig. 4c,d) confirming that NO
391 signaling does not influence resting vascular tone. Similar to NOS inhibition by L-NAME, ODQ
392 dramatically altered the overall vascular response (-27.6 ± 10.2 %.min, p= 0.02253, Fig. 4c and
393 d1) and reduced the magnitude (3.0 ± 1.2%, p=0.00093, Fig. 4d2) and maximal amplitude of
394 vasodilation (0.9 ± 0.3 %, p= 0.00172, Fig. 4d3). It also strongly delayed the vasodilation onset
395 (1119 ± 216 s, p= 0.00130, Fig. 4e1), and reduced its duration (147 ± 58 s, p= 0.00123, Fig. 4e3)
396 without impacting the time to peak of vasodilation (1119 ± 216 s, Fig. 4e2). In contrast to L-
397 NAME treatment, ODQ, did not alter the magnitude, amplitude, or kinetic properties of
398 vasoconstrictive events (Supplementary Fig. 4g1-5). Taken together, these results indicate

399 that AP firing is mandatory for the vasodilation evoked by 2 Hz photostimulation, which is
400 mediated by NO synthesis and signaling. Furthermore, they show that 2 Hz optogenetic
401 stimulation induces vasoconstriction that is masked by NO-dependent vasodilation.
402
403 **NPY-induced vasoconstriction involves the Y1 receptor independently of spiking activity.**
404 Since the majority of Sst interneurons are positive for NPY (Fig. 3b1,2) and virtually all cortical
405 type 1 NO-producing interneurons express this neuropeptide (Dawson et al., 1991; Estrada
406 and DeFelipe, 1998; Kubota et al., 1994, 2011; Perrenoud et al., 2012a), NPY could be
407 responsible for the vasoconstriction observed with 20 Hz photostimulation, but also with 2 Hz
408 photostimulation under NOS inhibition. We first verified that NPY induced vasoconstriction in
409 a dose-dependent manner (Supplementary Fig. 5). 10 nM NPY (n= 11 arterioles) evoked very
410 small vasoconstriction (Supplementary Fig. 5b e1-3), that only differed form control condition
411 (n= 3 arterioles) for their onset (10 nM: 548 ± 194 s, p= 0.04430, Supplementary Fig. 5f1). 100
412 nM (n= 10 arterioles) and 1 µM NPY (n= 9 arterioles) evoked much stronger vasoconstriction,
413 as evidenced by their magnitude (100 nM: -154.9 ± 40.7 %.min, p= 0.01154; 1 µM: -162.5 ±
414 23.0 %.min, p= 0.00474, Supplementary Fig. 5e1), maximal amplitude (100 nM: -13.1 ± 2.2 %,
415 p= 0.02023; 1 µM: -25.1 ± 3.4 %, p= 0.00062, Supplementary Fig. 5e2). Vasoconstriction
416 evoked by 100 nM and 1 µM occurred also much faster (100 nM: 282 ± 43 s, p= 0.04430; 1µM:
417 147 ± 18 s, p= 0.00281, Supplementary Fig. 5e3) and time to peak (100 nM: 545 ± 116 s, p=
418 0.02912; 1µM: 311 ± 38 s, p= 0.00395, Supplementary Fig. 5e4). They also lasted longer (998 ±
419 124 s, p= 0.01731; 1µM: 1234 ± 104s, p= 0.00113, Supplementary Fig. 5e5). Since the
420 vasoconstriction induced by 20 Hz optogenetic stimulation of Sst-ChR2 and 100 nM NPY were
421 of similar magnitude and maximal amplitude (Fig. 2f2,3 and supplementary Fig. 5e1,2) we next
422 evaluated whether the NPY Y1 antagonist BIBP3226 could abolish the vasoconstriction
423 induced by 100 nM. Pretreatment with BIBP3226 (1µM (Perrenoud et al., 2012b), n= 10
424 arterioles) dramatically reduced the vasoconstriction induced by 100 nM NPY (Fig. 5a), as
425 evidenced by its effect on the magnitude (-8.0 ± 7.6 %.min, p= 0.00181, Fig. 5c1) and maximum
426 amplitude (-0.8 ± 0.7 %, p= 0.00144, Fig. 5c2). BIBP3226 also dramatically delayed the onset
427 (1486 ± 212 s, p= 0.01467, Fig. 5c3) and time to peak (1622 ± 137 s, p= 0.00207, Fig. 5c4) of
428 NPY-induced vasoconstriction and reduced its duration (175 ± 148 s, p= 0.01261, Fig. 5c5).
429 These observations confirm that NPY induces strong arteriolar vasoconstriction via Y1
430 receptors. Since Y1 receptor is expressed by smooth muscle cells (Vanlandewijck et al., 2018;

431 Zhang et al., 2024) but also by neurons (Smith et al., 2019; Tasic et al., 2016; Zeisel et al., 2015)
432 it has been proposed that NPY-induced vasoconstriction could be mediated by intermediary
433 neuronal types (Kaplan et al., 2020). To rule out this possibility we investigated the impact of
434 AP firing inhibition on NPY-induced vasoconstriction. We found that TTX treatment (1 µM, n=
435 9 arterioles) had no effect on the magnitude (-173.7 ± 58.8 %.min, p= 0.62911, Fig. 5c1),
436 maximum amplitude (-14.3 ± 4.2 %, p= 0.64910, Fig. 5c2), onset (554 ± 239s, p= 0.88537, Fig.
437 5c3), time to peak (752 ± 211 s, p= 0.45002, Fig. 5c4) and duration (903 ± 199s, p= 0.80606,
438 Fig. 2c5) of vasoconstriction induced by 100 nM NPY. Collectively these observations indicate
439 that NPY induces vasoconstriction via the Y1 receptor independently of neuronal activity.
440

441 **Vasoconstriction induced by 20 Hz photostimulation of Sst-ChR2 interneurons requires AP**
442 **firing and NPY Y1 signaling**

443 To investigate the mechanisms responsible for the vasoconstriction induced by 20 Hz
444 optogenetic stimulation of Sst-ChR2 interneurons, we first evaluated the requirement of AP
445 firing. TTX treatment (1µM, n= 10 arterioles) dramatically reduced the magnitude (-14.1 ± 5.8,
446 %.min, p= 0.01810, Fig. 6a, c2), maximum amplitude (-1.9 ± 0.5 %, p= 0.00092, Fig. 6c3) of
447 vasoconstriction induced by 20 Hz photostimulation. It also delayed the vasoconstriction
448 onset (990 ± 236 s, p= 0.01993, Fig. 6d1) without significantly altering its apparent time to
449 peak (1163 ± 187 s, Fig. 6d2) and duration (571 ± 196 s, Fig. 6d3). TTX had also no impact on
450 vasodilatory events evoked by 20 Hz photostimulation (Supplementary Fig. 6c1-5). These
451 observations indicate that AP firing is mandatory for vasoconstriction induced by 20 Hz
452 optogenetic stimulation of Sst-ChR2 interneurons. We next investigated whether this vascular
453 response could be mediated by NPY. Antagonizing Y1 receptor in Sst-ChR2 slices with
454 BIBP3226 (1µM, n=10 arterioles) did not alter the arteriolar diameter (diameter before: 17.1
455 ± 2.0 µm *vs.* after BIBP3226: 17.0 ± 2.0 µm, $t_{(9)}$= 0.82945, p= 0.4283, Supplementary Fig. 6a,b)
456 indicating that tonic NPY level does not influence resting vascular tone. In contrast, BIBP3226
457 dramatically reduced the magnitude (-21.8 ± 8.6 %.min, p= 0.01810, Fig. 6a,c2) and the
458 maximum amplitude (-2.0 ± 0.6 %, p= 0.00092, Fig. 6c3) of vasoconstriction induced by 20 Hz
459 optogenetic stimulation. It also delayed the onset of vasoconstriction (934 ± 244 s, p= 0.01993,
460 Fig 6d1) without altering its time to peak (1148 ± 201s, Fig. 6d2) and duration (643 ± 224s, Fig.
461 6d3). Similar to TTX, BIBP3226 had no impact on the vasodilatory events induced by 20 Hz
462 Photostimulation (Supplementary Fig. 6c1-5). Taken together, these observations indicate

463 that vasoconstriction induced by 20 Hz photostimulation of Sst-ChR2 neurons requires both
464 AP firing and NPY signaling through the Y1 receptor.
465
466
467

468 **DISCUSSION**

469 Here we used optogenetics in mouse cortical slices to show that Sst interneurons exert a
470 bimodal vascular response that requires AP firing and whose polarity depends on the
471 stimulation frequency. The vasodilation induced by 2 Hz photostimulation involves NO
472 synthesis and signaling via the sGC, whereas the vasoconstriction induced by 20 Hz
473 photostimulation implies NPY and activation of its Y1 receptor. Consistently, histochemical
474 investigations revealed that subpopulations of photostimulated Sst interneurons express the
475 NOS-1 and/or NPY (Fig. 7).

476

477 **Frequency dependence of the neuronal and vascular responses**

478 The observation that Sst interneurons respond supralinearly to low-frequency optogenetic
479 stimulation is reminiscent of the higher impedance observed at low frequency in hippocampal
480 Sst-positive oriens lacunosum-moleculare cells (Zemankovics et al., 2010), which depends on
481 a high capacitance and a pronounced hyperpolarisation-activated cation current I_h, two
482 features shared by cortical Sst interneurons (Halabisky et al., 2006; Karagiannis et al., 2009,
483 2021; Perrenoud et al., 2012a). Indeed, according to Ohm's law, a higher impedance at low
484 frequency would have resulted in a larger voltage response induced by the ChR2
485 photocurrents, resulting in a higher number of spikes per light pulse. We found that depending
486 on the AP firing frequency, Sst interneurons can induce vasodilation or vasoconstriction. These
487 results confirm and extend our previous observations in rat cortical slices showing that the
488 evoked firing of single Sst interneurons at a frequency of at least 8 Hz results in
489 vasoconstriction (Cauli et al., 2004). Similarly, the *in vivo* optogenetic stimulation of GABAergic
490 interneurons was found to induce hyperemia/vasodilation, which can be followed by
491 vasoconstriction (Anenberg et al., 2015; Uhlirova et al., 2016). In addition, photostimulation
492 of Sst interneurons also induced a hyperemic response, followed by a decrease in blood flow
493 that became more pronounced with increasing duration of stimulation (Krawchuk et al., 2019;
494 Lee et al., 2020). Our findings are further supported by the observations showing that the
495 selective optogenetic, chemogenetic or pharmacological stimulation of NOS-1 expressing Sst
496 interneurons induced hyperemia/vasodilation (Echagarruga et al., 2020; Ruff et al., 2024) also
497 support our findings. Nevertheless compared to those *in vivo,* the responses we observed in
498 slices were notably much slower and longer lasting (Krawchuk et al., 2019; Lee et al., 2020).
499 This is likely due to the lower temperature in *ex vivo* experiments which has been reported to

500 slowdown the synthesis of vasoactive messenger (Rancillac et al., 2006) and subsequent
501 reactions. In contrast to *in vivo* observations (Uhlirova et al., 2016; Krawchuk et al., 2019; Lee
502 et al., 2020), the *ex vivo* magnitude of vasoconstriction was greater than that of vasodilation.
503 Here, the absence of vascular tone in slices, which favors vasoconstriction (Blanco et al.,
504 2008), probably led to an underestimation of vasodilation. On the other hand the absence of
505 blood flow in the slices may have reduced the scavenging of NO by hemoglobin (Rancillac et
506 al., 2006), whose *in vivo* concentration locally increases during functional hyperemia (Devor
507 et al., 2007; Lee et al., 2020), thereby prolonging *ex vivo* vasodilation.
508
509 **Cellular and molecular mechanisms of vasodilation and vasoconstriction.**
510 We found that the vasodilation induced by the 2 Hz optogenetic stimulation was dependent
511 on AP firing, NO synthesis and activation of soluble guanylate cyclase (sGC). The mandatory
512 role of APs indicates that Ca^{2+} entry via ChR2 alone is insufficient to drive vasodilation. This
513 likely reflects the essential role of voltage-gated Ca^{2+} channels in somatic Ca^{2+} elevation (Mao
514 et al., 2001) and the subsequent Ca^{2+}-dependent activation of NOS-1, NO release and
515 vasodilation (Rancillac et al., 2006; Attwell et al., 2010; Cauli and Hamel, 2010; Iadecola, 2017;
516 Cauli and Hamel, 2018). Consistently, some supragranular NOS-1 neurons showed an increase
517 in somatic Ca^{2+} prior to vasodilation evoked by whisker stimulation and/or spontaneous
518 locomotion in awake head-fixed mice whereas others showed a gradual and delayed
519 activation (Ahn et al., 2023). Although type 1 NOS-1 interneurons are preferentially located in
520 deep layers (Perrenoud et al., 2012a), our histochemical observations revealed the presence
521 of NOS-1 positive Sst-Cre interneurons in superficial layers. Together with the high excitability
522 of Sst interneurons (Karagiannis et al., 2009, 2021; Perrenoud et al., 2012a), these
523 observations suggest that some of these interneurons correspond to the fast responder NOS-
524 1 neurons (Ahn et al., 2023). The abolition of the optogenetically induced vasodilation evoked
525 by 2 Hz photostimulation by both NOS and sGC inhibition strongly suggests that it is mediated
526 by NO synthesis, release and direct action on smooth muscle cells, leading to their relaxation
527 (Fig. 7). However, NOS inhibition revealed a vasoconstriction, most likely mediated by NPY
528 (Uhlirova et al., 2016), that was not observed when sGC or AP firing was blocked. These
529 observations suggest that a NO-sensitive, but soluble guanylate cyclase-independent,
530 mechanism of vasodilation counterbalanced the vasoconstriction disclosed by L-NAME. Active
531 astrocytes, which have been shown to produce vasodilatory epoxyeicosatrienoic acids via the

532 P450 epoxygenase (Alkayed et al., 1997), might be responsible for such a vasodilation. Indeed,
533 astrocytes are reported to be robustly activated by the repetitive firing of Sst interneurons
534 (Mariotti et al., 2018), and the P450 expoygenase is inhibited by NO (Roman, 2002; Metea and
535 Newman, 2006; Attwell et al., 2010).
536 We found that vasoconstriction predominates over vasodilation when Sst-ChR2 interneurons
537 are photostimulated at 20 Hz. This reflects the much higher number of NPY-positive Sst-ChR2
538 interneurons compared to type 1 NOS-1 interneurons (Karagiannis et al., 2009; Perrenoud et
539 al., 2012a) and the dense network of NPY positive terminals on blood vessels (Abounader and
540 Hamel, 1997). Furthermore, the release of NPY from large dense-core vesicles requires a
541 higher firing frequency than the release of neurotransmitters from synaptic vesicles (Baraban
542 and Tallent, 2004). It is also possible that the release of NO requires a lower firing frequency
543 than that of NPY. We found that optogenetically induced vasoconstriction was almost
544 completely abolished by the antagonism of Y1 receptors, suggesting that this effect was
545 essentially mediated by NPY, as reported for the optogenetic stimulation of GABAergic
546 interneurons (Uhlirova et al., 2016). We cannot exclude the indirect contribution of Sst and
547 GABA which can exert vasoconstrictive effects (Long et al., 1992; Fergus and Lee, 1997).
548 Indeed, the repetitive firing of Sst interneurons robustly activates astrocytes via Sst and $GABA_B$
549 receptors (Mariotti et al., 2018), which could in turn induce vasoconstriction via 20-
550 hydroxyeicosatetraenoic acid (Mulligan and MacVicar, 2004) and/or K+ (Girouard et al., 2010).
551 However, Sst is not as efficient as NPY in inducing vasoconstriction in cortical slices (Cauli et
552 al., 2004), and the amount of Sst in the cerebral cortex is reduced in Sst-Cre mice (Viollet et
553 al., 2017), but not that of NPY. On the other hand, the vasoconstrictor effect of the $GABA_B$
554 receptor activation requires AP firing (Fergus and Lee, 1997), suggesting that it is mediated by
555 neurons and not by astrocytes. Thus, it is more likely that the vasoconstriction induced by 20
556 Hz optogenetic stimulation of Sst-ChR2 interneurons is essentially mediated by NPY and the
557 Y1 receptors.
558
559 **Physiological relevance of the bidirectional control of neurovascular coupling by Sst-**
560 **interneurons**
561 The ability of Sst interneurons to drive a bimodal vascular response *ex vivo* depending on firing
562 frequency is consistent with *in vivo* observations showing that increasing the duration and/or
563 the frequency of photostimulation of Sst-ChR2 interneurons favors the observation of

564 decreased blood flow, in addition to hyperemia (Krawchuk et al., 2019; Lee et al., 2020).
565 However, the evoked decrease in blood flow appears to be more pronounced at a site
566 different from the site of hyperemia (Lee et al., 2020). This is reminiscent of the
567 center/surround pattern of vasodilation/vasoconstriction observed *in vivo* in response to
568 sensory stimulation, with the vasodilation in the activated area preceding the peripheral
569 vasoconstriction (Devor et al., 2007; Boorman et al., 2010; Uhlirova et al., 2016). Because fast-
570 responding NOS-1 neurons are activated before the onset of vasodilation (Ahn et al., 2023),
571 they are most likely involved in the initiation of vasodilation. Consistently, local NO production
572 precedes functional hyperemia but disappears before the end of stimulation (Buerk et al.,
573 2003), presumably because of the short half-life of NO (Wood and Garthwaite, 1994) and its
574 increased scavenging induced by functional hyperemia. The delayed and/or peripheral
575 vasoconstriction (Devor et al., 2007; Uhlirova et al., 2016; Krawchuk et al., 2019; Lee et al.,
576 2020) could be due to its blunting by early occurring vasodilation, a higher level of activity
577 required for NPY release (Baraban and Tallent, 2004), as suggested by our observations,
578 and/or a different site of action of NO and NPY (Estrada and DeFelipe, 1998).
579 Sst/NOS-1/NPY neurons largely correspond to long-range GABAergic neurons (Tomioka et al.,
580 2005) and have been shown to locally induce vasodilation (Echagarruga et al., 2020; Ruff et
581 al., 2024). It remains to determine whether their interhemispheric long-range projection (Ruff
582 et al., 2024) could explain the vasoconstriction observed contralaterally to the activated area
583 (Devor et al., 2008) when their activity is elevated. Sst/NOS-1/NPY also correspond to cortical
584 sleep active neurons (Gerashchenko et al., 2008; Kilduff et al., 2011). Furthermore, Sst and
585 Sst/NOS-1 interneurons are involved in slow and delta wave activities, respectively (Morairty
586 et al., 2013; Funk et al., 2017; Zielinski et al., 2019), a frequency range associated with sleep
587 that we showed was the most efficient at activating them. Interestingly, oscillating
588 vasodilation of large amplitude and a vasoconstriction are observed during non REM sleep and
589 upon awakening, respectively (Turner et al., 2020; Bojarskaite et al., 2023). Whether the
590 coordinated action of NO and NPY could participate in these hemodynamic changes in a
591 frequency-dependent manner remains also to be determined.
592
593 **Bidirectional control of neurovascular coupling by Sst interneurons in pathological**
594 **conditions**

595 Several neurological disorders, such as epilepsy (Sada et al., 2015; Gaxiola-Valdez et al., 2017)
596 or Alzheimer's disease (Palop et al., 2007; Kimbrough et al., 2015; Le Douce J. et al., 2020),
597 associate hyperactivity with gliovascular and metabolic deficits that are likely to alter the
598 control of neurovascular coupling by Sst interneurons. For example, cerebral lactate, which is
599 produced by astrocytes from glucose during excitatory transmission (Pellerin and Magistretti,
600 1994; Cauli et al., 2023), is dramatically increased in epilepsy (Slais et al., 2008). Drugs that
601 interfere with lactate metabolism by neurons have emerged as a promising strategy for
602 treating epilepsy (Sada et al., 2015), an effect that involves the neuronal uptake of lactate, its
603 oxidative metabolism and the subsequent closure of ATP-sensitive potassium channels. Since
604 Sst interneurons functionally express these channels (Karagiannis et al., 2021) and are among
605 the neurons showing the highest mitochondrial content (Gulyas et al., 2006), their activity is
606 likely to be efficiently enhanced by the presence of lactate and its oxidative metabolism. This
607 could favor the GABAergic inhibition of pyramidal cells (Silberberg and Markram, 2007), but
608 also decreased glutamatergic transmission (Bacci et al., 2002), and Y1-mediated
609 vasoconstriction (Uhlirova et al., 2016), thereby mitigating lactate-induced hyperactivity (Sada
610 et al., 2015).
611 Hyperactivity has also been reported in several models of Alzheimer's disease (Palop et al.,
612 2007; Bezzina et al., 2015; Zott et al., 2019), and loss of Sst interneurons has been observed
613 in patients (Gaspar et al., 1989) and in the early stages of a mouse model of the disease (Ramos
614 et al., 2006). Furthermore, Sst/NOS-1/NPY interneurons play a key role in non-REM sleep
615 (Gerashchenko et al., 2008; Morairty et al., 2013; Zielinski et al., 2019), during which the
616 fluctuations in the perivascular space favor the clearance of β-amyloid peptides (Iliff et al.,
617 2013; Xie et al., 2013; Bojarskaite et al., 2023). These observations suggest that the control of
618 NVC by Sst interneurons may be altered early, accelerating amyloid plaque accumulation and
619 disease progression. However, NVC has been shown to be impaired (Kimbrough et al., 2015;
620 Lourenco et al., 2017), unchanged (Sharp et al., 2020) or even enhanced (Shabir et al., 2020;
621 Kim et al., 2024), making it difficult to assess its alterations. Whether these differences depend
622 on the mouse model, the stage of disease progression, or the experimental condition remains
623 to be investigated.
624
625 **Conclusion**

626 Here, using a combination of approaches, we describe the mechanisms by which Sst
627 interneurons bidirectionally control NVC as a function of their firing frequency. Vasodilation
628 was preferentially evoked at low-frequency photostimulation and primarily involves NO
629 release and activation of its vascular receptor sGC. In contrast, vasoconstriction was more
630 reliably induced at high frequency and involves NPY release and activation of the vascular
631 receptor Y1. This finding will help to update the interpretation of the functional brain imaging
632 signals used to map network activity in health and disease (Iadecola, 2017; Zhang and Raichle,
633 2010). This bimodal control of neurovascular coupling may also help to define therapeutic
634 targets for epilepsy and Alzheimer's disease in which hyperactivity, gliovascular and metabolic
635 deficits overlap (Palop and Mucke, 2010; Sada et al., 2015; Gaxiola-Valdez et al., 2017).
636

637 **Data availability statement**

638 The data that support the results of this study are available from the corresponding author
639 upon reasonable request.
640

641 **Competing interests**

642 The authors declare no competing interests.
643

644 **Acknowledgements**

645 We acknowledge the invaluable support of the animal (RongIBPS) and imaging facilities of the
646 IBPS. Financial support was provided by grants from the Agence Nationale de la Recherche
647 (ANR-17-CE37-0010-03, B.C.; ANR-20-CE14-0025, D.L.; ANR-23-CE14-0038-01, B.C.), and the i-
648 Bio initiative of Sorbonne University (B.C.). B.M was supported by a fellowship form Centre
649 National de la Recherche Scientifique. B.L.G. and E.B. were supported by fellowships from
650 Fondation pour la Recherche sur Alzheimer.
651

652 **Author contributions**

653 B.M., J.O.R, S.P. B.L.G., M.T., and E.B. designed experiments, acquired and analyzed the data,
654 and edited the manuscript. B.M. and B.C. drafted the manuscript. L.R.V.C. edited the
655 manuscript. I.D. designed experiments and edited the manuscript. H.S. analyzed the data. D.L.
656 provided resources and edited the manuscript. B.C. designed experiments, analyzed the data
657 and edited the manuscript.

658

659

660 **REFERENCES**

661 Abounader R, Hamel E. 1997. Associations between neuropeptide Y nerve terminals and
662 intraparenchymal microvessels in rat and human cerebral cortex. *JComp Neurol* **388**:444–
663 453.
664 Ahn SJ, Anfray A, Anrather J, Iadecola C. 2023. Calcium transients in nNOS neurons underlie distinct
665 phases of the neurovascular response to barrel cortex activation in awake mice. *J Cereb*
666 *Blood Flow Metab* **43**:1633–1647. doi:10.1177/0271678X231173175
667 Alkayed NJ, Birks EK, Narayanan J, Petrie KA, Kohler-Cabot AE, Harder DR. 1997. Role of P-450
668 arachidonic acid epoxygenase in the response of cerebral blood flow to glutamate in rats.
669 *Stroke* **28**:1066–1072.
670 Anenberg E, Chan AW, Xie Y, LeDue JM, Murphy TH. 2015. Optogenetic stimulation of GABA neurons
671 can decrease local neuronal activity while increasing cortical blood flow. *JCerebBlood Flow*
672 *Metab*.
673 Ascoli GA, Alonso-Nanclares L, Anderson SA, Barrionuevo G, avides-Piccione R, Burkhalter A, Buzsaki
674 G, Cauli B, DeFelipe J, Fairen A, Feldmeyer D, Fishell G, Fregnac Y, Freund TF, Gardner D,
675 Gardner EP, Goldberg JH, Helmstaedter M, Hestrin S, Karube F, Kisvarday ZF, Lambolez B,
676 Lewis DA, Marin O, Markram H, Munoz A, Packer A, Petersen CC, Rockland KS, Rossier J, Rudy
677 B, Somogyi P, Staiger JF, Tamas G, Thomson AM, Toledo-Rodriguez M, Wang Y, West DC,
678 Yuste R. 2008. Petilla terminology: nomenclature of features of GABAergic interneurons of
679 the cerebral cortex. *NatRevNeurosci* **9**:557–568.
680 Attwell D, Buchan AM, Charpak S, Lauritzen M, MacVicar BA, Newman EA. 2010. Glial and neuronal
681 control of brain blood flow. *Nature* **468**:232–243.
682 Bacci A, Huguenard JR, Prince D a. 2002. Differential modulation of synaptic transmission by
683 neuropeptide Y in rat neocortical neurons. *Proc Natl Acad Sci U S A* **99**:17125–30.
684 doi:10.1073/pnas.012481899
685 Baraban SC, Tallent MK. 2004. Interneuron Diversity series: Interneuronal neuropeptides--
686 endogenous regulators of neuronal excitability. *Trends Neurosci* **27**:135–142.
687 Benjamini Y, Hochberg Y. 1995. Controlling the False Discovery Rate: A Practical and Powerful
688 Approach to Multiple Testing. *J R Stat Soc Ser B Stat Methodol* **57**:289–300.
689 doi:10.1111/j.2517-6161.1995.tb02031.x
690 Bezzina C, Verret L, Juan C, Remaud J, Halley H, Rampon C, Dahan L. 2015. Early Onset of
691 Hypersynchronous Network Activity and Expression of a Marker of Chronic Seizures in the
692 Tg2576 Mouse Model of Alzheimer's Disease. *PLOS ONE* **10**:e0119910.
693 doi:10.1371/journal.pone.0119910
694 Blanco VM, Stern JE, Filosa JA. 2008. Tone-dependent vascular responses to astrocyte-derived
695 signals. *AmJPhysiol Heart CircPhysiol* **294**:H2855–H2863.
696 Bojarskaite L, Vallet A, Bjørnstad DM, Gullestad Binder KM, Cunen C, Heuser K, Kuchta M, Mardal K-
697 A, Enger R. 2023. Sleep cycle-dependent vascular dynamics in male mice and the predicted
698 effects on perivascular cerebrospinal fluid flow and solute transport. *Nat Commun* **14**:953.
699 doi:10.1038/s41467-023-36643-5
700 Boorman L, Kennerley AJ, Johnston D, Jones M, Zheng Y, Redgrave P, Berwick J. 2010. Negative blood
701 oxygen level dependence in the rat: a model for investigating the role of suppression in
702 neurovascular coupling. *JNeurosci* **30**:4285–4294.
703 Buerk DG, Ances BM, Greenberg JH, Detre JA. 2003. Temporal dynamics of brain tissue nitric oxide
704 during functional forepaw stimulation in rats. *Neuroimage* **18**:1–9.
705 Cauli B, Audinat E, Lambolez B, Angulo MC, Ropert N, Tsuzuki K, Hestrin S, Rossier J. 1997. Molecular
706 and physiological diversity of cortical nonpyramidal cells. *JNeurosci* **17**:3894–3906.

707 Cauli B, Dusart I, Li D. 2023. Lactate as a determinant of neuronal excitability, neuroenergetics and
708 beyond. *Neurobiol Dis* **184**:106207. doi:10.1016/j.nbd.2023.106207
709 Cauli B, Hamel E. 2018. Brain Perfusion and Astrocytes. *Trends Neurosci* **41**:409–413.
710 Cauli B, Hamel E. 2010. Revisiting the role of neurons in neurovascular coupling. *Front*
711 *Neuroenergetics* **2**:9.
712 Cauli B, Tong XK, Rancillac A, Serluca N, Lambolez B, Rossier J, Hamel E. 2004. Cortical GABA
713 interneurons in neurovascular coupling: relays for subcortical vasoactive pathways. *JNeurosci*
714 **24**:8940–8949.
715 Choi M, Yoon J, Choi C. 2010. Label-free optical control of arterial contraction. *JBiomedOpt*
716 **15**:015006.
717 Dawson TM, Bredt DS, Fotuhi M, Hwang PM, Snyder SH. 1991. Nitric oxide synthase and neuronal
718 NADPH diaphorase are identical in brain and peripheral tissues. *ProcNatlAcadSciUSA*
719 **88**:7797–7801.
720 DeFelipe J, Lopez-Cruz PL, avides-Piccione R, Bielza C, Larranaga P, Anderson S, Burkhalter A, Cauli B,
721 Fairen A, Feldmeyer D, Fishell G, Fitzpatrick D, Freund TF, Gonzalez-Burgos G, Hestrin S, Hill S,
722 Hof PR, Huang J, Jones EG, Kawaguchi Y, Kisvarday Z, Kubota Y, Lewis DA, Marin O, Markram
723 H, McBain CJ, Meyer HS, Monyer H, Nelson SB, Rockland K, Rossier J, Rubenstein JL, Rudy B,
724 Scanziani M, Shepherd GM, Sherwood CC, Staiger JF, Tamas G, Thomson A, Wang Y, Yuste R,
725 Ascoli GA. 2013. New insights into the classification and nomenclature of cortical GABAergic
726 interneurons. *NatRevNeurosci*. doi:10.1038/nrn3444
727 Devienne G, Le Gac B, Piquet J, Cauli B. 2018. Single Cell Multiplex Reverse Transcription Polymerase
728 Chain Reaction After Patch-clamp. *JVisExp*.
729 Devor A, Hillman EM, Tian P, Waeber C, Teng IC, Ruvinskaya L, Shalinsky MH, Zhu H, Haslinger RH,
730 Narayanan SN, Ulbert I, Dunn AK, Lo EH, Rosen BR, Dale AM, Kleinfeld D, Boas DA. 2008.
731 Stimulus-induced changes in blood flow and 2-deoxyglucose uptake dissociate in ipsilateral
732 somatosensory cortex. *JNeurosci* **28**:14347–14357.
733 Devor A, Tian P, Nishimura N, Teng IC, Hillman EM, Narayanan SN, Ulbert I, Boas DA, Kleinfeld D, Dale
734 AM. 2007. Suppressed neuronal activity and concurrent arteriolar vasoconstriction may
735 explain negative blood oxygenation level-dependent signal. *JNeurosci* **27**:4452–4459.
736 Dodt HU, Zieglgansberger W. 1998. Visualization of neuronal form and function in brain slices by
737 infrared videomicroscopy. *HistochemJ* **30**:141–152.
738 Drew PJ. 2022. Neurovascular coupling: motive unknown. *Trends Neurosci* **45**:809–819.
739 Echagarruga CT, Gheres KW, Norwood JN, Drew PJ. 2020. nNOS-expressing interneurons control
740 basal and behaviorally evoked arterial dilation in somatosensory cortex of mice. *Elife* **9**.
741 Estrada C, DeFelipe J. 1998. Nitric oxide-producing neurons in the neocortex: morphological and
742 functional relationship with intraparenchymal microvasculature. *CerebCortex* **8**:193–203.
743 Fergus A, Lee KS. 1997. GABAergic regulation of cerebral microvascular tone in the rat. *JCerebBlood*
744 *Flow Metab* **17**:992–1003.
745 Funk CM, Peelman K, Bellesi M, Marshall W, Cirelli C, Tononi G. 2017. Role of Somatostatin-Positive
746 Cortical Interneurons in the Generation of Sleep Slow Waves. *JNeurosci* **37**:9132–9148.
747 Gaspar P, Duyckaerts C, Febvret A, Benoit R, Beck B, Berger B. 1989. Subpopulations of somatostatin
748 28-immunoreactive neurons display different vulnerability in senile dementia of the
749 Alzheimer type. *Brain Res* **490**:1–13.
750 Gaxiola-Valdez I, Singh S, Perera T, Sandy S, Li E, Federico P. 2017. Seizure onset zone localization
751 using postictal hypoperfusion detected by arterial spin labelling MRI. *Brain* **140**:2895–2911.
752 Gerashchenko D, Wisor JP, Burns D, Reh RK, Shiromani PJ, Sakurai T, de la I, Kilduff TS. 2008.
753 Identification of a population of sleep-active cerebral cortex neurons. *ProcNatlAcadSciUSA*.
754 Girouard H, Bonev AD, Hannah RM, Meredith A, Aldrich RW, Nelson MT. 2010. Astrocytic endfoot
755 Ca2+ and BK channels determine both arteriolar dilation and constriction.
756 *ProcNatlAcadSciUSA* **107**:3811–3816.
757 Gulyas AI, Buzsaki G, Freund TF, Hirase H. 2006. Populations of hippocampal inhibitory neurons
758 express different levels of cytochrome c. *EurJNeurosci* **23**:2581–2594.

759 Halabisky BE, Shen F, Huguenard JR, Prince DA. 2006. Electrophysiological Classification of
760 Somatostatin-positive Interneurons in Mouse Sensorimotor Cortex. *JNeurophysiol*.
761 Hartmann DA, Berthiaume AA, Grant RI, Harrill SA, Koski T, Tieu T, McDowell KP, Faino AV, Kelly AL,
762 Shih AY. 2021. Brain capillary pericytes exert a substantial but slow influence on blood flow.
763 *NatNeurosci* **24**:633–645.
764 Hendry SH, Jones EG, Emson PC. 1984. Morphology, distribution, and synaptic relations of
765 somatostatin- and neuropeptide Y-immunoreactive neurons in rat and monkey neocortex.
766 *JNeurosci* **4**:2497–2517.
767 Hepp R, Tricoire L, Hu E, Gervasi N, Paupardin-Tritsch D, Lambolez B, Vincent P. 2007.
768 Phosphodiesterase type 2 and the homeostasis of cyclic GMP in living thalamic neurons.
769 *JNeurochem* **102**:1875–1886.
770 Hill RA, Tong L, Yuan P, Murikinati S, Gupta S, Grutzendler J. 2015. Regional Blood Flow in the Normal
771 and Ischemic Brain Is Controlled by Arteriolar Smooth Muscle Cell Contractility and Not by
772 Capillary Pericytes. *Neuron* **87**:95–110.
773 Hu H, Cavendish JZ, Agmon A. 2013. Not all that glitters is gold: off-target recombination in the
774 somatostatin-IRES-Cre mouse line labels a subset of fast-spiking interneurons. *Front Neural*
775 *Circuits* **7**:195.
776 Iadecola C. 2017. The Neurovascular Unit Coming of Age: A Journey through Neurovascular Coupling
777 in Health and Disease. *Neuron* **96**:17–42.
778 Iliff JJ, Wang M, Zeppenfeld DM, Venkataraman A, Plog BA, Liao Y, Deane R, Nedergaard M. 2013.
779 Cerebral Arterial Pulsation Drives Paravascular CSF-Interstitial Fluid Exchange in the Murine
780 Brain. *JNeurosci* **33**:18190–18199.
781 Kaplan L, Chow BW, Gu C. 2020. Neuronal regulation of the blood-brain barrier and neurovascular
782 coupling. *NatRevNeurosci* **21**:416–432.
783 Karagiannis A, Gallopin T, David C, Battaglia D, Geoffroy H, Rossier J, Hillman EM, Staiger JF, Cauli B.
784 2009. Classification of NPY-expressing neocortical interneurons. *JNeurosci* **29**:3642–3659.
785 Karagiannis A, Gallopin T, Lacroix A, Plaisier F, Piquet J, Geoffroy H, Hepp R, Naude J, Le GB, Egger R,
786 Lambolez B, Li D, Rossier J, Staiger JF, Imamura H, Seino S, Roeper J, Cauli B. 2021. Lactate is
787 an energy substrate for rodent cortical neurons and enhances their firing activity. *Elife*
788 **10**:e71424.
789 Kilduff TS, Cauli B, Gerashchenko D. 2011. Activation of cortical interneurons during sleep: an
790 anatomical link to homeostatic sleep regulation? *Trends Neurosci* **34**:10–19.
791 Kim TA, Cruz G, Syty MD, Wang F, Wang X, Duan A, Halterman M, Xiong Q, Palop JJ, Ge S. 2024.
792 Neural circuit mechanisms underlying aberrantly prolonged functional hyperemia in young
793 Alzheimer's disease mice. *Mol Psychiatry*. doi:10.1038/s41380-024-02680-9
794 Kimbrough IF, Robel S, Roberson ED, Sontheimer H. 2015. Vascular amyloidosis impairs the
795 gliovascular unit in a mouse model of Alzheimer's disease. *Brain* **138**:3716–3733.
796 Krawchuk MB, Ruff CF, Yang X, Ross SE, Vazquez AL. 2019. Optogenetic assessment of VIP, PV, SOM
797 and NOS inhibitory neuron activity and cerebral blood flow regulation in mouse somato-
798 sensory cortex 1. *JCerebBlood Flow Metab* 271678X19870105.
799 Krogsgaard A, Sperling L, Dahlqvist M, Thomsen K, Vydmantaite G, Li F, Thunemann M, Lauritzen M,
800 Lind BL. 2023. PV interneurons evoke astrocytic Ca(2+) responses in awake mice, which
801 contributes to neurovascular coupling. *Glia*.
802 Kubota Y, Hattori R, Yui Y. 1994. Three distinct subpopulations of GABAergic neurons in rat frontal
803 agranular cortex. *Brain Res* **649**:159–173.
804 Kubota Y, Shigematsu N, Karube F, Sekigawa A, Kato S, Yamaguchi N, Hirai Y, Morishima M,
805 Kawaguchi Y. 2011. Selective coexpression of multiple chemical markers defines discrete
806 populations of neocortical GABAergic neurons. *CerebCortex* **21**:1803–1817.
807 Lacroix A, Toussay X, Anenberg E, Lecrux C, Ferreirós N, Karagiannis A, Plaisier F, Chausson P, Jarlier F,
808 Burgess SA, Hillman EMC, Tegeder I, Murphy TH, Hamel E, Cauli B. 2015. COX-2-Derived
809 Prostaglandin E2 Produced by Pyramidal Neurons Contributes to Neurovascular Coupling in

810 the Rodent Cerebral Cortex. *J Neurosci Off J Soc Neurosci* **35**:11791–11810.
811 doi:10.1523/JNEUROSCI.0651-15.2015
812 Le Douce J., Maugard M, Veran J, Matos M, Jego P, Vigneron PA, Faivre E, Toussay X, Vandenberghe
813 M, Balbastre Y, Piquet J, Guiot E, Tran NT, Taverna M, Marinesco S, Koyanagi A, Furuya S,
814 Gaudin-Guerif M, Goutal S, Ghettas A, Pruvost A, Bemelmans AP, Gaillard MC, Cambon K,
815 Stimmer L, Sazdovitch V, Duyckaerts C, Knott G, Herard AS, Delzescaux T, Hantraye P,
816 Brouillet E, Cauli B, Oliet SHR, Panatier A, Bonvento G. 2020. Impairment of Glycolysis-
817 Derived l-Serine Production in Astrocytes Contributes to Cognitive Deficits in Alzheimer's
818 Disease. *Cell Metab* **31**:503–517.
819 Lee L, Boorman L, Glendenning E, Christmas C, Sharp P, Redgrave P, Shabir O, Bracci E, Berwick J,
820 Howarth C. 2020. Key Aspects of Neurovascular Control Mediated by Specific Populations of
821 Inhibitory Cortical Interneurons. *CerebCortex* **30**:2452–2464.
822 Lee S, Hjerling-Leffler J, Zagha E, Fishell G, Rudy B. 2010. The largest group of superficial neocortical
823 GABAergic interneurons expresses ionotropic serotonin receptors. *JNeurosci* **30**:16796–
824 16808.
825 Lin JY, Lin MZ, Steinbach P, Tsien RY. 2009. Characterization of engineered channelrhodopsin variants
826 with improved properties and kinetics. *BiophysJ* **96**:1803–1814.
827 Long JB, Rigamonti DD, Dosaka K, Kraimer JM, Martinez-Arizala A. 1992. Somatostatin causes
828 vasoconstriction, reduces blood flow and increases vascular permeability in the rat central
829 nervous system. *JPharmacolExpTher* **260**:1425–1432.
830 Lourenco CF, Ledo A, Barbosa RM, Laranjinha J. 2017. Neurovascular uncoupling in the triple
831 transgenic model of Alzheimer's disease: Impaired cerebral blood flow response to neuronal-
832 derived nitric oxide signaling. *ExpNeurol* **291**:36–43.
833 Lovick TA, Brown LA, Key BJ. 1999. Neurovascular relationships in hippocampal slices: physiological
834 and anatomical studies of mechanisms underlying flow-metabolism coupling in
835 intraparenchymal microvessels. *Neuroscience* **92**:47–60.
836 Madisen L, Garner AR, Shimaoka D, Chuong AS, Klapoetke NC, Li L, van der BA, Niino Y, Egolf L,
837 Monetti C, Gu H, Mills M, Cheng A, Tasic B, Nguyen TN, Sunkin SM, Benucci A, Nagy A,
838 Miyawaki A, Helmchen F, Empson RM, Knopfel T, Boyden ES, Reid RC, Carandini M, Zeng H.
839 2015. Transgenic mice for intersectional targeting of neural sensors and effectors with high
840 specificity and performance. *Neuron* **85**:942–958.
841 Madisen L, Mao T, Koch H, Zhuo JM, Berenyi A, Fujisawa S, Hsu YW, Garcia AJ III, Gu X, Zanella S,
842 Kidney J, Gu H, Mao Y, Hooks BM, Boyden ES, Buzsaki G, Ramirez JM, Jones AR, Svoboda K,
843 Han X, Turner EE, Zeng H. 2012. A toolbox of Cre-dependent optogenetic transgenic mice for
844 light-induced activation and silencing. *NatNeurosci* **15**:793–802. doi:10.1038/nn.3078
845 Mao BQ, Hamzei-Sichani F, Aronov D, Froemke RC, Yuste R. 2001. Dynamics of spontaneous activity
846 in neocortical slices. *Neuron* **32**:883–898.
847 Mariotti L, Losi G, Lia A, Melone M, Chiavegato A, Gomez-Gonzalo M, Sessolo M, Bovetti S, Forli A,
848 Zonta M, Requie LM, Marcon I, Pugliese A, Viollet C, Bettler B, Fellin T, Conti F, Carmignoto G.
849 2018. Interneuron-specific signaling evokes distinctive somatostatin-mediated responses in
850 adult cortical astrocytes. *NatCommun* **9**:82.
851 Metea MR, Newman EA. 2006. Glial cells dilate and constrict blood vessels: a mechanism of
852 neurovascular coupling. *JNeurosci* **26**:2862–2870.
853 Morairty SR, Dittrich L, Pasumarthi RK, Valladao D, Heiss JE, Gerashchenko D, Kilduff TS. 2013. A role
854 for cortical nNOS/NK1 neurons in coupling homeostatic sleep drive to EEG slow wave activity.
855 *Proc Natl Acad Sci* **110**:20272–20277. doi:10.1073/pnas.1314762110
856 Mulligan SJ, MacVicar BA. 2004. Calcium transients in astrocyte endfeet cause cerebrovascular
857 constrictions. *Nature* **431**:195–199.
858 Palop JJ, Chin J, Roberson ED, Wang J, Thwin MT, Bien-Ly N, Yoo J, Ho KO, Yu GQ, Kreitzer A,
859 Finkbeiner S, Noebels JL, Mucke L. 2007. Aberrant excitatory neuronal activity and
860 compensatory remodeling of inhibitory hippocampal circuits in mouse models of Alzheimer's
861 disease. *Neuron* **55**:697–711.

862 Palop JJ, Mucke L. 2010. Amyloid-beta-induced neuronal dysfunction in Alzheimer's disease: from
863 synapses toward neural networks. *NatNeurosci* **13**:812–818.
864 Pellerin L, Magistretti PJ. 1994. Glutamate uptake into astrocytes stimulates aerobic glycolysis: a
865 mechanism coupling neuronal activity to glucose utilization. *ProcNatlAcadSciUSA* **91**:10625–
866 9.
867 Perrenoud Q, Geoffroy H, Gauthier B, Rancillac A, Alfonsi F, Kessaris N, Rossier J, Vitalis T, Gallopin T.
868 2012a. Characterization of Type I and Type II nNOS-Expressing Interneurons in the Barrel
869 Cortex of Mouse. *Front Neural Circuits* **6**:36. doi:10.3389/fncir.2012.00036
870 Perrenoud Q, Rossier J, Ferezou I, Geoffroy H, Gallopin T, Vitalis T, Rancillac A. 2012b. Activation of
871 cortical 5-HT(3) receptor-expressing interneurons induces NO mediated vasodilatations and
872 NPY mediated vasoconstrictions. *Front Neural Circuits* **6**:50. doi:10.3389/fncir.2012.00050
873 Price CJ, Cauli B, Kovacs ER, Kulik A, Lambolez B, Shigemoto R, Capogna M. 2005. Neurogliaform
874 neurons form a novel inhibitory network in the hippocampal CA1 area. *JNeurosci* **25**:6775–
875 6786.
876 Ramos B, Baglietto-Vargas D, del Rio JC, Moreno-Gonzalez I, Santa-Maria C, Jimenez S, Caballero C,
877 Lopez-Tellez JF, Khan ZU, Ruano D, Gutierrez A, Vitorica J. 2006. Early neuropathology of
878 somatostatin/NPY GABAergic cells in the hippocampus of a PS1xAPP transgenic model of
879 Alzheimer's disease. *NeurobiolAging* **27**:1658–1672.
880 Rancillac A, Rossier J, Guille M, Tong XK, Geoffroy H, Amatore C, Arbault S, Hamel E, Cauli B. 2006.
881 Glutamatergic Control of Microvascular Tone by Distinct GABA Neurons in the Cerebellum.
882 *JNeurosci* **26**:6997–7006.
883 Roman RJ. 2002. P-450 metabolites of arachidonic acid in the control of cardiovascular function.
884 *Physiol Rev* **82**:131–185.
885 Ruff CF, Juarez AF, Dienel SJ, Rakymzhan A, tamirano-Espinoza A, Couey J, Fukuda M, Watson AM, Su
886 A, Fish KN, Rubio ME, Hooks BM, Ross SE, Vazquez AL. 2024. Long-range inhibitory neurons
887 mediate cortical neurovascular coupling. *Cell Rep* **43**:113970.
888 Rungta RL, Chaigneau E, Osmanski BF, Charpak S. 2018. Vascular Compartmentalization of Functional
889 Hyperemia from the Synapse to the Pia. *Neuron* **99**:362–375.
890 Rungta RL, Osmanski BF, Boido D, Tanter M, Charpak S. 2017. Light controls cerebral blood flow in
891 naive animals. *NatCommun* **8**:14191.
892 Sada N, Lee S, Katsu T, Otsuki T, Inoue T. 2015. Targeting LDH enzymes with a stiripentol analog to
893 treat epilepsy. *Science* **347**:1362–1367. doi:10.1126/science.aaa1299
894 Schaeffer S, Iadecola C. 2021. Revisiting the neurovascular unit. *NatNeurosci* **24**:1198–1209.
895 Shabir O, Sharp P, Rebollar MA, Boorman L, Howarth C, Wharton SB, Francis SE, Berwick J. 2020.
896 Enhanced Cerebral Blood Volume under Normobaric Hyperoxia in the J20-hAPP Mouse
897 Model of Alzheimer's Disease. *SciRep* **10**:7518.
898 Sharp PS, Ameen-Ali KE, Boorman L, Harris S, Wharton S, Howarth C, Shabir O, Redgrave P, Berwick J.
899 2020. Neurovascular coupling preserved in a chronic mouse model of Alzheimer's disease:
900 Methodology is critical. *J Cereb Blood Flow Metab Off J Int Soc Cereb Blood Flow Metab*
901 **40**:2289–2303. doi:10.1177/0271678X19890830
902 Silberberg G, Markram H. 2007. Disynaptic inhibition between neocortical pyramidal cells mediated
903 by Martinotti cells. *Neuron* **53**:735–746.
904 Slais K, Vorisek I, Zoremba N, Homola A, Dmytrenko L, Sykova E. 2008. Brain metabolism and
905 diffusion in the rat cerebral cortex during pilocarpine-induced status epilepticus. *ExpNeurol*
906 **209**:145–154.
907 Smith SJ, Sumbul U, Graybuck LT, Collman F, Seshamani S, Gala R, Gliko O, Elabbady L, Miller JA,
908 Bakken TE, Rossier J, Yao Z, Lein E, Zeng H, Tasic B, Hawrylycz M. 2019. Single-cell
909 transcriptomic evidence for dense intracortical neuropeptide networks. *Elife* **8**.
910 Sun X, Li P, Luo W, Chen S, Feng N, Wang J, Luo Q. 2010. Investigating the effects of
911 dimethylsulfoxide on hemodynamics during cortical spreading depression by combining laser
912 speckle imaging with optical intrinsic signal imaging. *Lasers SurgMed* **42**:649–655.

913 Taniguchi H, He M, Wu P, Kim S, Paik R, Sugino K, Kvitsiani D, Fu Y, Lu J, Lin Y, Miyoshi G, Shima Y,
914 Fishell G, Nelson SB, Huang ZJ. 2011. A resource of Cre driver lines for genetic targeting of
915 GABAergic neurons in cerebral cortex. *Neuron* **71**:995–1013.
916 doi:10.1016/j.neuron.2011.07.026
917 Tasic B, Menon V, Nguyen TN, Kim TK, Jarsky T, Yao Z, Levi B, Gray LT, Sorensen SA, Dolbeare T,
918 Bertagnolli D, Goldy J, Shapovalova N, Parry S, Lee C, Smith K, Bernard A, Madisen L, Sunkin
919 SM, Hawrylycz M, Koch C, Zeng H. 2016. Adult mouse cortical cell taxonomy revealed by
920 single cell transcriptomics. *NatNeurosci* **19**:335–346.
921 Thevenaz P, Ruttimann UE, Unser M. 1998. A pyramid approach to subpixel registration based on
922 intensity. *IEEE TransImage Process* **7**:27–41.
923 Tomioka R, Okamoto K, Furuta T, Fujiyama F, Iwasato T, Yanagawa Y, Obata K, Kaneko T, Tamamaki
924 N. 2005. Demonstration of long-range GABAergic connections distributed throughout the
925 mouse neocortex. *EurJNeurosci* **21**:1587–1600.
926 Tricoire L, Kubota Y, Cauli B. 2013. Cortical NO interneurons: from embryogenesis to functions. *Front*
927 *Neural Circuits* **7**:105.
928 Tricoire L, Pelkey KA, Daw MI, Sousa VH, Miyoshi G, Jeffries B, Cauli B, Fishell G, McBain CJ. 2010.
929 Common origins of hippocampal ivy and nitric oxide synthase expressing neurogliaform cells.
930 *JNeurosci* **30**:2165–2176.
931 Turner KL, Gheres KW, Proctor EA, Drew PJ. 2020. Neurovascular coupling and bilateral connectivity
932 during NREM and REM sleep. *eLife* **9**:e62071. doi:10.7554/eLife.62071
933 Uhlirova H, Kilic K, Tian P, Thunemann M, Desjardins M, Saisan PA, Sakadzic S, Ness TV, Mateo C,
934 Cheng Q, Weldy KL, Razoux F, Vanderberghe M, Cremonesi JA, Ferri CG, Nizar K, Sridhar VB,
935 Steed TC, Abashin M, Fainman Y, Masliah E, Djurovic S, Andreassen O, Silva GA, Boas DA,
936 Kleinfeld D, Buxton RB, Einevoll GT, Dale AM, Devor A. 2016. Cell type specificity of
937 neurovascular coupling in cerebral cortex. *Elife* **5**:e14315.
938 Vanlandewijck M, He L, Mae MA, Andrae J, Ando K, Del GF, Nahar K, Lebouvier T, Lavina B, Gouveia L,
939 Sun Y, Raschperger E, Rasanen M, Zarb Y, Mochizuki N, Keller A, Lendahl U, Betsholtz C. 2018.
940 A molecular atlas of cell types and zonation in the brain vasculature. *Nature* **554**:475–480.
941 Viollet C, Simon A, Tolle V, Labarthe A, Grouselle D, Loe-Mie Y, Simonneau M, Martel G, Epelbaum J.
942 2017. Somatostatin-IRES-Cre Mice: Between Knockout and Wild-Type? *Front*
943 *EndocrinolLausanne* **8**:131.
944 Wood J, Garthwaite J. 1994. Models of the diffusional spread of nitric oxide: implications for neural
945 nitric oxide signalling and its pharmacological properties. *Neuropharmacology* **33**:1235–1244.
946 Xie L, Kang H, Xu Q, Chen MJ, Liao Y, Thiyagarajan M, O'Donnell J, Christensen DJ, Nicholson C, Iliff JJ,
947 Takano T, Deane R, Nedergaard M. 2013. Sleep drives metabolite clearance from the adult
948 brain. *Science* **342**:373–377.
949 Zeisel A, Manchado AB, Codeluppi S, Lonnerberg P, La MG, Jureus A, Marques S, Munguba H, He L,
950 Betsholtz C, Rolny C, Castelo-Branco G, Hjerling-Leffler J, Linnarsson S. 2015. Cell types in the
951 mouse cortex and hippocampus revealed by single-cell RNA-seq. *Science* **347**:1138–1142.
952 Zemankovics R, Kali S, Paulsen O, Freund TF, Hajos N. 2010. Differences in subthreshold resonance of
953 hippocampal pyramidal cells and interneurons: the role of h-current and passive membrane
954 characteristics. *JPhysiol* **588**:2109–2132.
955 Zhang D, Raichle ME. 2010. Disease and the brain's dark energy. *NatRevNeurol* **6**:15–28.
956 Zhang D, Ruan J, Peng S, Li J, Hu X, Zhang Y, Zhang T, Ge Y, Zhu Z, Xiao X, Zhu Y, Li X, Li T, Zhou L, Gao
957 Q, Zheng G, Zhao B, Li X, Zhu Y, Wu J, Li W, Zhao J, Ge WP, Xu T, Jia JM. 2024. Synaptic-like
958 transmission between neural axons and arteriolar smooth muscle cells drives cerebral
959 neurovascular coupling. *NatNeurosci*.
960 Zielinski MR, Atochin DN, McNally JM, McKenna JT, Huang PL, Strecker RE, Gerashchenko D. 2019.
961 Somatostatin+/nNOS+ neurons are involved in delta electroencephalogram activity and
962 cortical-dependent recognition memory. *Sleep* **42**.

Zonta M, Angulo MC, Gobbo S, Rosengarten B, Hossmann KA, Pozzan T, Carmignoto G. 2003. Neuron-to-astrocyte signaling is central to the dynamic control of brain microcirculation. *NatNeurosci* **6**:43–50.

Zott B, Simon MM, Hong W, Unger F, Chen-Engerer HJ, Frosch MP, Sakmann B, Walsh DM, Konnerth A. 2019. A vicious cycle of beta amyloid-dependent neuronal hyperactivation. *Science* **365**:559–565.

FIGURE LEGEND

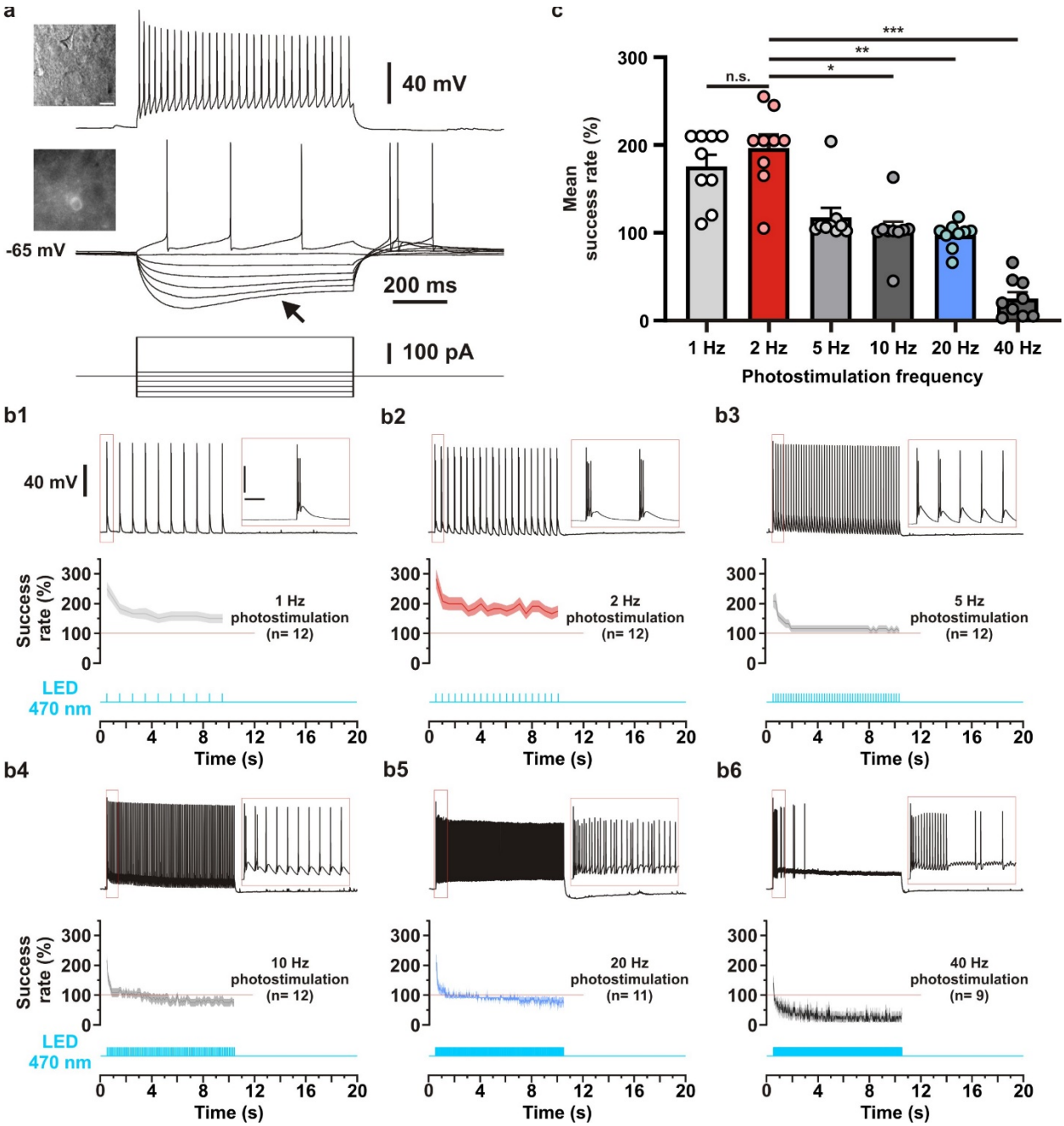

Figure 1: Electrophysiological characterization of cortical Sst-ChR2 neurons. (a) Representative recording showing the voltage responses induced by 800 ms current injections (bottom traces) of -100 pA, -80 pA, -60 pA, -40 pA, -20 pA, 0 pA, +15 and +150 pA in a cortical EYFP/ChR2-expressing neuron from a Sst-Cre:Ai32 mouse. Note the pronounced voltage sag after the initial peak response (arrow) to

977 hyperpolarizing current injections (middle traces). Just-above threshold current pulse (+15 pA)
978 triggered a discharge of three action potentials (middle traces). Note the complex AHP consisting of a
979 fast AHP, a small ADP, and a medium AHP. Near saturation, a strong depolarizing current (+150 pA)
980 elicited a discharge of action potentials with a marked frequency adaptation and a monotonous
981 amplitude accommodation (upper trace). Top inset: IR videomicroscopy picture of the recorded
982 neuron, the pial surface is upward (scale bar, 20 µm). Bottom insets, corresponding field of view
983 showing the EYFP fluorescence of the recorded neuron. **(b1-6)** Voltage responses (upper traces) of the
984 Sst-ChR2 neuron shown in **(a)** induced by photostimulations (470 nm, 10 s train, 5 ms pulses) delivered
985 at 1, 2, 5, 10, 20 and 40 Hz (cyan lower traces) and instantaneous spike success rate (middle trace).
986 The red boxes highlight the first second of the zoomed recording in the right insets (scaled bars 200
987 ms, 40 mV). The red lines represent a spike success rate of 100%. Note that more than one action
988 potential is elicited per light pulse delivered at 1 or 2 Hz whereas at frequencies above 5 Hz this success
989 rate rapidly decreases to a maximum of one spike per light pulse. (**c**) Histogram showing the average
990 spike success rate induced by photostimulations at 1, 2, 5, 10, 20, or 40 Hz (n = 9 Sst-ChR2 cortical
991 neurons from 6 SST-Cre:Ai32 mice). Note the average spike success rate exceeding 100 % at
992 photostimulation frequencies lower than 10 Hz. Data are presented as means ± SEM. The SEMs
993 envelope the mean traces Statistically different with *p< 0.05, **p< 0.01 and ***p< 0.001; n.s.: not
994 statistically significant.
995

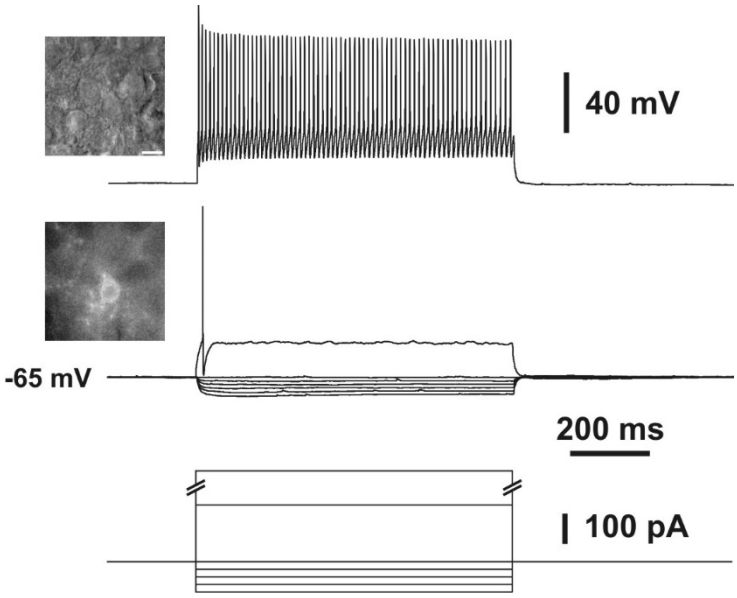

996
997
998 **Supplementary Figure 1: Electrophysiological characterization of a fast spiking Sst-ChR2 neurons.**
999 Recording showing the voltage responses induced by 800 ms current injections (bottom traces) of -
1000 100 pA, -80 pA, -60 pA, -40 pA, -20 pA, 0 pA, +190 and +600 pA in a cortical EYFP/ChR2-expressing
1001 neuron of a Sst-Cre:Ai32 mouse. Note the small voltage response to hyperpolarizing current injections
1002 (middle traces). Just-above threshold current pulse (+190 pA) triggered a discharge of an action
1003 potential (middle traces). Note the sharp and fast AHP. Near saturation, a strong depolarizing current
1004 (+600 pA) triggered a discharge of action potentials with a weak frequency adaptation and a
1005 monotonous amplitude accommodation. Top inset: IR videomicroscopy picture of the recorded
1006 neuron, the pial surface is upward (scale bar, 20 µm). Bottom insets, corresponding field of view
1007 showing the EYFP fluorescence of the recorded neuron.
1008

1009 **Supplementary Table 1. Electrophysiological properties of Sst-ChR2 interneuron**

	Adapting-*Sst* (n= 15)	Fast Spiking (n=1)
Passive properties		
(1) Resting potential (mV)	-59.5 ± 4.5	-58.0
(2) Input resistance (MΩ)	608 ± 231	129
(3) Time constant (ms)	39.1 ± 15.3	11.7
(4) Membrane capacitance (pF)	68.5 ± 31.1	90.7
(5) Sag index (%)	21.2 ± 10.6	10.5
Just above threshold properties		
(6) Rheobase (pA)	8 ± 14	187
(7) First spike latency (ms)	130.1 ± 162.8	17.0
(8) Adaptation (Hz/s)	-2.6 ± 6.9	-38.5
(9) Minimal frequency (Hz)	9.3 ± 6.7	41.4
Firing properties		
(10) Accommodation (mV)	0.7 ± 0.7	0.2
(11) Amplitude of early adaptation (Hz)	27.1 ± 10.0	30.4
(12) Time constant of early adaptation (ms)	60.5 ± 23.8	15.2
(13) Late adaptation (Hz/s)	-10.3 ± 9.4	-21.7
(14) Maximal frequency (Hz)	46.7 ± 16.6	98.6
Action potentials properties		
(15) 1st spike amplitude (mV)	83.6 ± 8.8	85.9
(16) 1st spike duration (ms)	1.3 ± 0.3	0.6
(17) 2nd spike amplitude (mV)	79.2 ± 9.1	78.3
(18) 2nd spike duration (ms)	1.4 ± 0.3	0.7
(19) Amplitude Reduction (%)	5.4 ± 3.9	8.9
(20) Duration Increase (%)	3.3 ± 3.8	6.3
AHP and ADP properties		
(21) 1st spike fast AHP (mV)	-18.6 ± 5.5	-26.5
(22) 1st spike ADP (mV)	2.2 ± 2.7	0.0
(23) 1st spike medium AHP (mV)	-7.5 ± 6.5	0.0
(24) 1st spike fast AHP latency (ms)	5.0 ± 1.4	2.6
(25) 1st spike ADP latency (ms)	8.5 ± 7.9	0.0
(26) 1st spike, medium AHP latency (ms)	18.5 ± 18.2	0.0
(27) 2nd spike fast AHP (mV)	-19.4 ± 6.0	-28.6
(28) 2nd spike ADP (mV)	2.0 ± 2.6	0.0
(29) 2nd spike medium AHP (mV)	-8.2 ± 7.2	0.0
(30) 2nd spike, fast AHP latency (ms)	5.2 ± 1.4	2.8
(31) 2nd spike ADP latency (ms)	8.7 ± 9.0	0.0
(32) 2nd spike, medium AHP latency (ms)	19.5 ± 19.0	0.0

1010

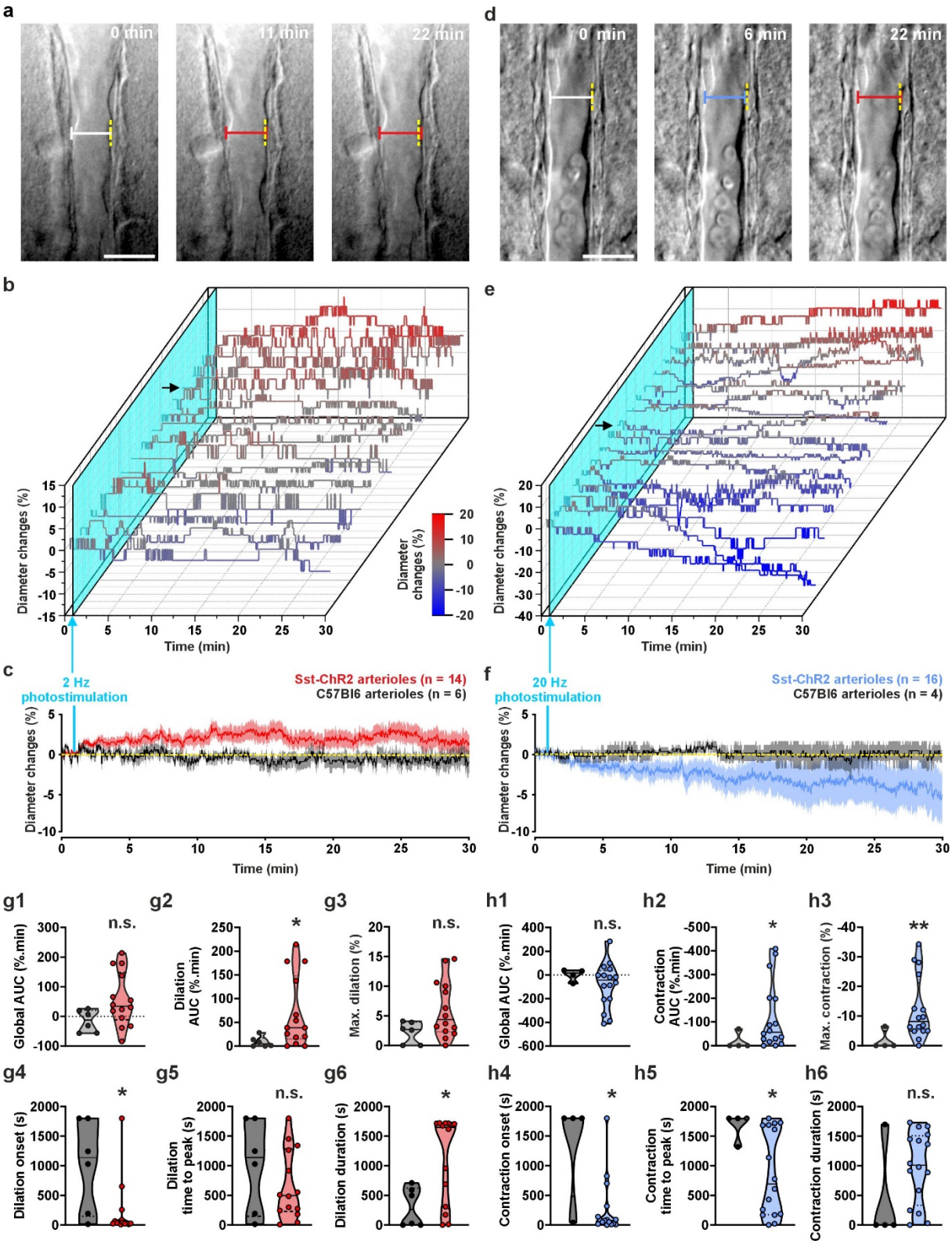

Figure 2: Bidirectional frequency-dependent vascular response induced by optogenetic stimulation of cortical Sst-ChR2 neurons. (a, d) Representative examples of infrared pictures of diving arterioles and diameter measurements before (0 min) and after (6, 11, 22 min) photostimulation at 2 Hz **(a)** and 20 Hz **(d)** in Sst-Cre:Ai32 cortical slices. The pial surface is upward. Scale bars 20 µm. **(a, d)** White, red and blue calipers correspond to baseline, dilated, and contracted arteriolar diameters, respectively. The dashed yellow lines indicate the initial diameters. Note the slight increase **(a)** and decrease followed by an increase **(d)** in diameter induced by photostimulation delivered at 2 Hz **(a)** and 20 Hz

(d), respectively. **(b, e)** Waterfall plots showing the kinetics of changes in diameter of single arterioles induced by photostimulation at 2 Hz **(b)** and 20 Hz **(e)**. The inset shows the color code used for constriction (blue) and dilation (red) used in both panels. Arterioles are sorted by increasing values of total vascular changes. The cyan planes and arrows indicate the onset of photostimulation. Black arrows indicate changes in diameter of the arterioles shown in **(a)** and **(b)**. **(c, f)** Kinetics of mean diameter changes induced by 2 Hz **(c)** or 20 Hz **(f)** photostimulation. The dashed yellow lines correspond to the initial diameters. **(c)** Note the average small diameter increase induced by 2 Hz photostimulation in Sst-Cre:Ai32 (red, n= 14 arterioles from 8 mice) but not in C57Bl6 arterioles (black, n= 6 arterioles from 5 mice) and **(f)** the average progressive diameter decrease induced by 20 Hz photostimulation in Sst-Cre:Ai32 (blue, n= 16 arterioles from 10 mice) but not in WT arterioles (black, n= 4 arterioles from 3 mice). **(g1-6, h1-6)** Violin plots summarizing the comparison of overall vascular response **(g1, h1)**, magnitude of dilation **(g2)** and contraction **(h2)**, maximum dilation **(g3)** and contraction **(h3)**, onset **(g4,h4)** time to peak **(g5,h5)** and duration **(g6,h6)** of dilation **(g2-6)** and contraction **(h2-6)** between arterioles from slices of Sst-Cre:Ai32 and C57Bl6 mice stimulated at 2 **(g1-6**) and 20 Hz **(h1-6)**. Note the larger **(g2),** earlier **(g4)** and longer **(g6)** dilation in Sst-ChR2 slices stimulated at 2 Hz and the larger **(h2,3)**, and earlier onset **(h4)** and time to peak **(h5)** contraction in Sst-ChR2 slices stimulated at 20 Hz Data are presented as individual values. Solid and dashed black bars correspond to median and quartile values. * and ** statistically different from C57Bl6 mice with $p < 0.05$ and 0.01, respectively. n.s.: not statistically significant.

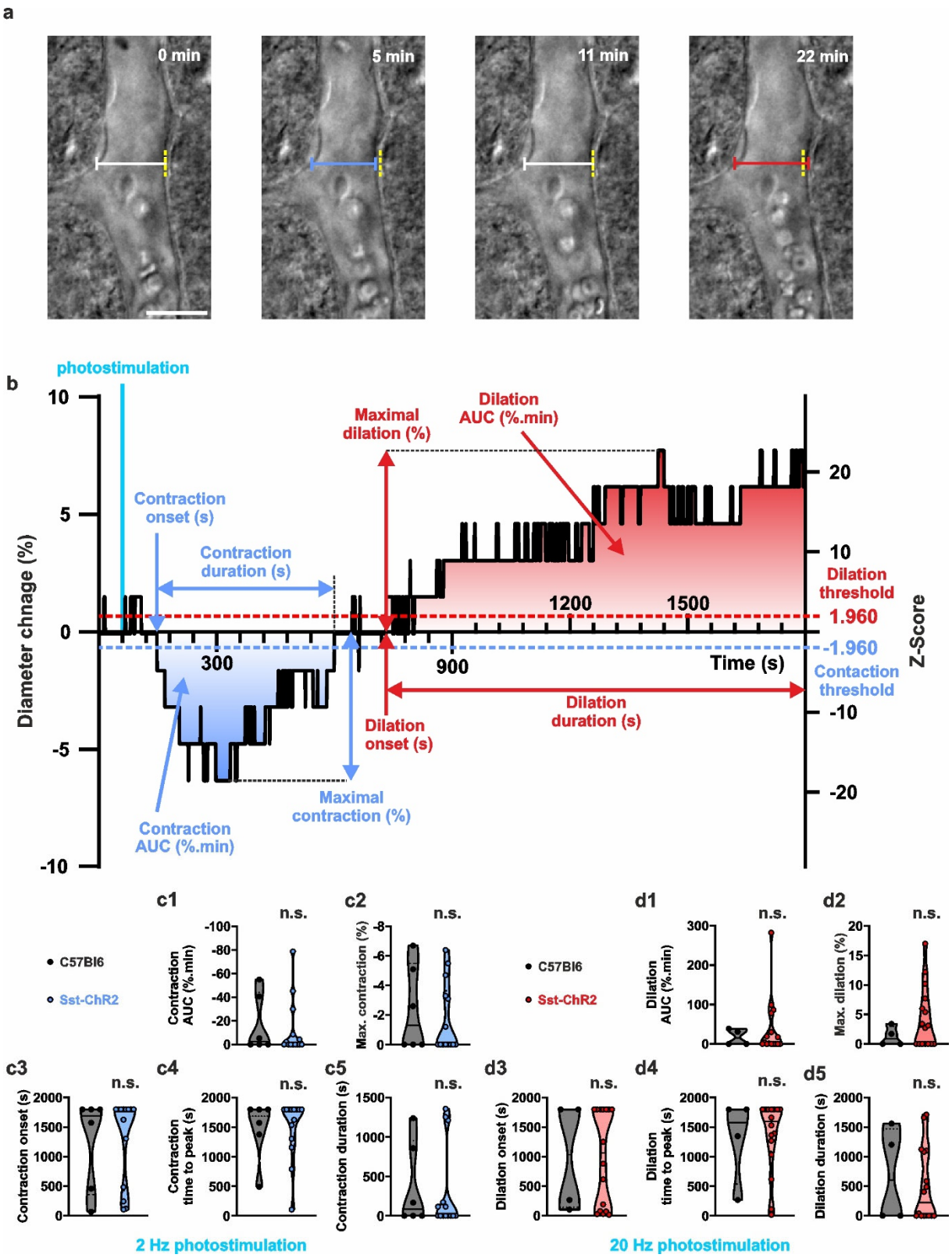
a
0 min
5 min
11 min
22 min
b
photostimulation
Diameter chnage (%)
Z-Score
Time (s)
Contraction onset (s)
Contraction duration (s)
Contraction AUC (%.min)
Maximal contraction (%)
Maximal dilation (%)
Dilation AUC (%.min)
Dilation onset (s)
Dilation duration (s)
Dilation threshold
1.960
-1.960
Contaction threshold
C57Bl6
Sst-ChR2
Contraction AUC (%.min)
Max. contraction (%)
Dilation AUC (%.min)
Max. dilation (%)
Contraction onset (s)
Contraction time to peak (s)
Contraction duration (s)
Dilation onset (s)
Dilation time to peak (s)
Dilation duration (s)
n.s.
2 Hz photostimulation
20 Hz photostimulation

1038

1039
1040 **Supplementary Figure 2: Measurement of vascular response parameters. (a)** Infrared pictures of a
1041 diving arteriole before (0 min) and after 20 Hz photostimulation showing a vasoconstriction (5 min)
1042 followed by a vasodilation (22 min). The pial surface is upward. Scale bars 20 µm. White, red and blue
1043 calipers correspond to the baseline, dilated, and contracted arteriolar diameter, respectively. The
1044 dashed yellow lines indicate the initial diameter. **(b)** Kinetics of the vascular response of the arteriole
1045 shown in **(a)** expressed as diameter changes (left axis) and Z-score (right axis) relative to the baseline
1046 period. The dashed horizontal blue and red lines depict the statistical ($p<0.05$) Z-score thresholds for
1047 contraction and dilation, respectively. The measured parameters include the onset, maximum
1048 amplitude, duration, and area under the curve of vascular responses. **(c1-5, d1-5)** Violin plots
1049 summarizing the comparison of magnitude of contraction **(c1)** and dilation**(d1)**, maximal contraction
1050 **(c2)** and dilation **(d2)**, onset **(c3,d3),** time to peak **(c4,f4)**, and duration **(c5,f5)** of contraction **(c1-5)** and
1051 dilation **(d1-5)** between arterioles from slices of Sst-Cre:Ai32 and C57Bl6 mice stimulated at 2 (**c1-5**)
1052 and 20 Hz (**d1-5**), respectively. Note that the vasoconstriction and vasodilation, respectively elicited by
1053 2 and 20 Hz stimulation of Sst-ChR2 slices, do not differ from the sporadic vascular changes observed
1054 in C57Bl6 slices. Data are presented as individual values. Solid and dashed black bars correspond to
1055 median and quartile values. n.s.: not statistically significant.
1056

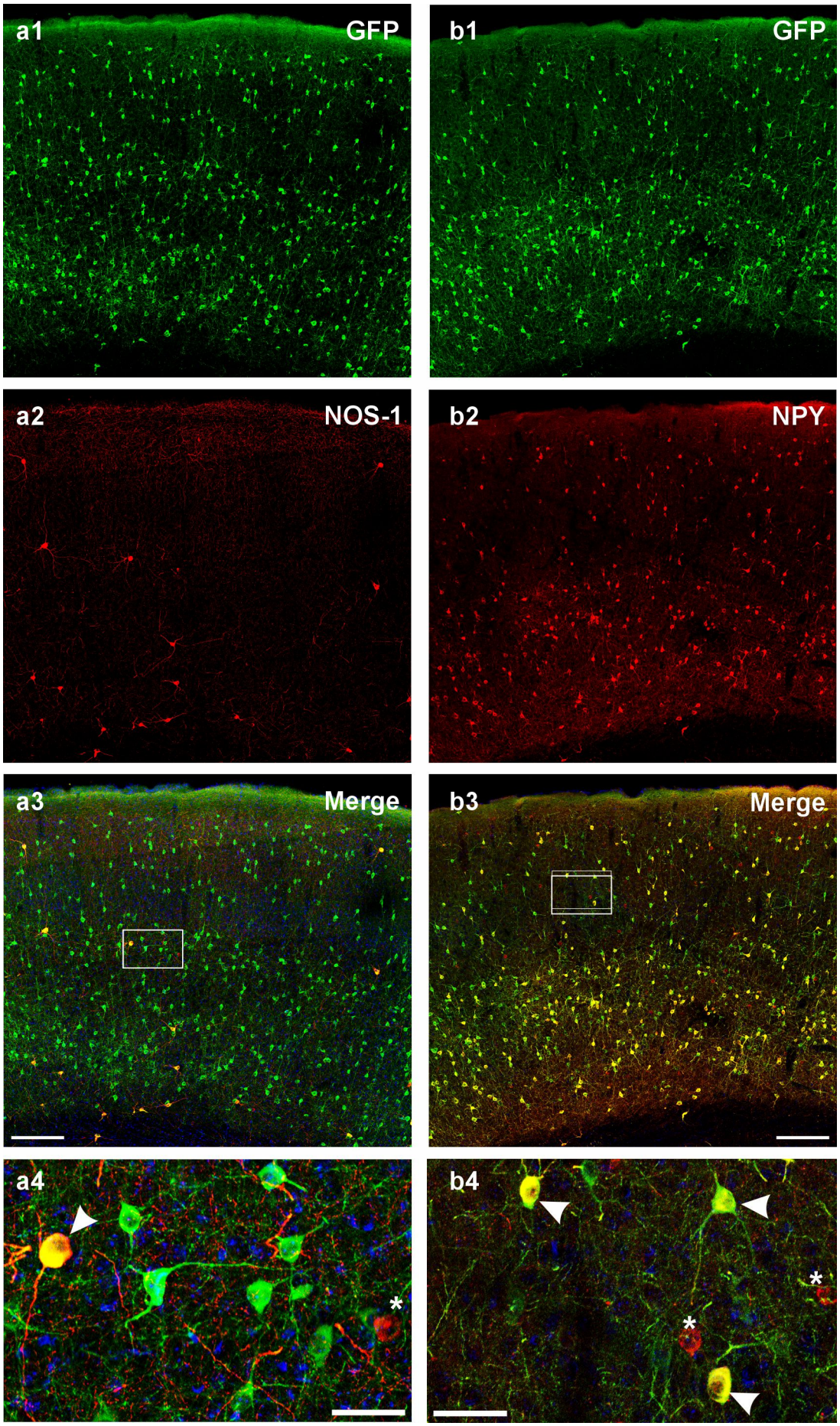

1057

1058 **Figure 3: Expression of NOS-1 and NPY in Sst-Cre neurons. (a1,b1)** Representative maximum intensity
1059 projections of 30 µm thick stacked confocal images showing GFP (green) expression in cortical slices
1060 from Sst-GCaMP6f mice. (**a2**) NOS-1 immunolabeling (red) is present in rare neurons. (**b2**) Numerous
1061 GFP-positive neurons are immunolabeled for NPY (red). (**a3,b3**) Double fluorescence images showing
1062 the co-expression of NOS-1 in rare GFP-positive neurons (a3) and NPY in numerous GFP positive
1063 neurons (b3). The white rectangles in **a3** and **b3** correspond to the zoomed regions shown in **a4** and
1064 **b4**, respectively. Arrowheads indicate GPF-positive neurons immunolabelled for NOS-1 (**a4**) or NPY
1065 (**b4)**. Asterisks denote GFP-negative neurons immunostained for NOS-1 (**a4**) or NPY (**b4**). Scale bars:
1066 200 µm (**a3, b3**) and 40 µm (**a4,b4**).
1067

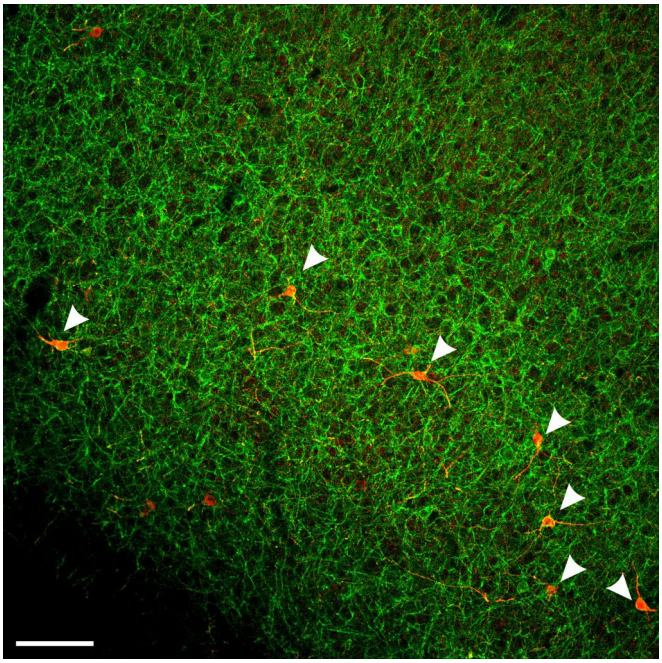

1068
1069
1070 **Supplementary Figure 3: Expression of NOS-1 in Sst-ChR2 neurons**. Single-plane confocal image of
1071 double-fluorescence staining showing the expression of ChR2-EYFP (green) and NOS-1 (red) in a
1072 cortical slice from a Sst-ChR2 mouse. Note the densely labeled ChR2-EYFP positive fibers and
1073 perikarions. Arrowheads indicate ChR2-EYFP-positive neurons immunolabelled for NOS-1. Scale bar:
1074 100 µm.
1075

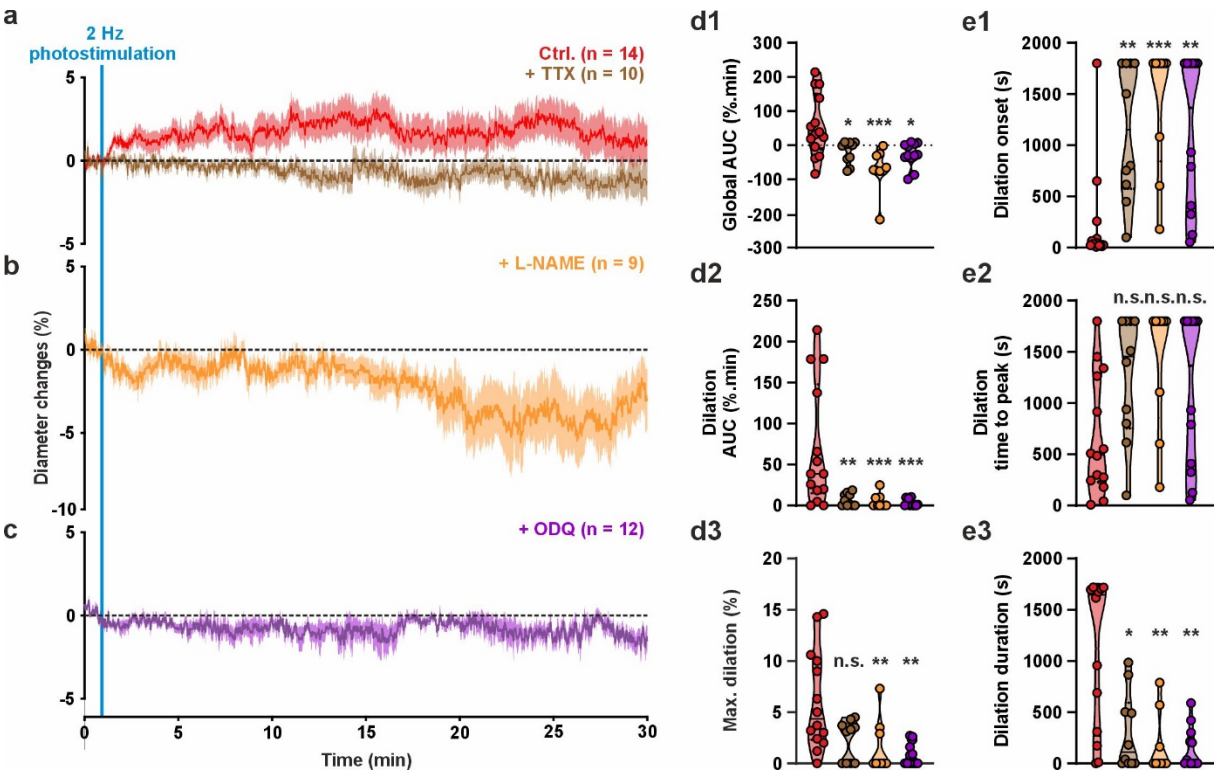

Figure 4: Vasodilation induced by 2 Hz photostimulation of Sst-ChR2 neurons requires spiking activity and nitric oxide signaling. **(a, b, c)** Effects of tetrodotoxin (TTX, 1 µM, brown, n= 10 arterioles from 6 mice), NOS inhibitor (L-NAME, orange, 100 µM, n= 9 arterioles from 6 mice) and ODQ (10 µM, purple, n= 12 arterioles from 7 mice), on the kinetics of the vascular response induced by 2 Hz photostimulation of Sst-ChR2 neurons. The red traces correspond to the control condition shown in Fig. 2b. The SEMs envelope the mean traces. Vasodilation is abolished by blocking action potentials with TTX **(a)**, inhibiting nitric oxide synthase with L-NAME **(b)** or sGC with ODQ **(c)**. The dashed black lines indicate the normalized initial diameters. Violin plots summarizing the effects of TTX (brown), L-NAME (orange) and ODQ (purple) on the overall vascular response **(d1**, $H_{(5,51)}$= 16.105, p= 0.00288**)**, magnitude **(d2**, $H_{(5,51)}$= 18.625, p= 0.00093**),** maximum **(d3**, $H_{(5,51)}$= 14.834, p=0.00506**)**, onset **(e1**, $H_{(5,51)}$= 20.592, p= 0.00038**),** time to peak **(e2**, $H_{(5,51)}$= 8.299, p= 0.08123**)**, and duration **(e3**, $H_{(5,51)}$= 16.867, p= 0.00205**)** of vasodilation induced by 2 Hz photostimulation (red). Data are presented as individual values. Solid and dashed black bars correspond to median and quartile values. * and ** statistically different from control condition with p<0.05 and 0.01 respectively.

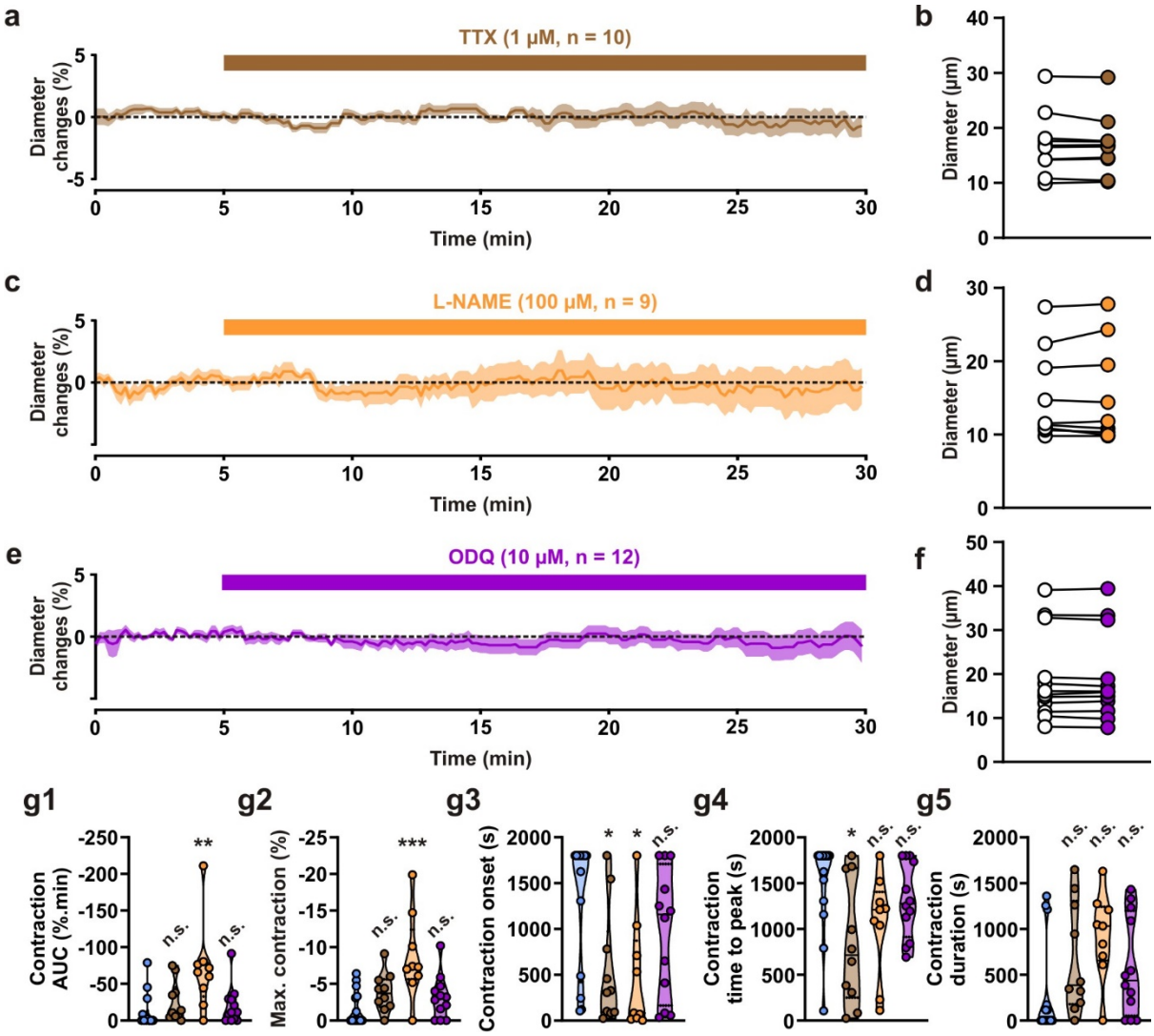

Supplementary Figure 4: Effects of pharmacological treatments on the basal vascular tone and the vasoconstriction evoked by 2 Hz stimulation. (a, c, e) Kinetics of vascular diameter changes during pharmacological application. Note the absence of diameter changes during the application of 1 µM TTX (**a**, brown horizontal zone, n= 10 arterioles from 6 mice), 100 µM L-NAME (**c**, blue horizontal zone, n= 9 arterioles from 6 mice) and 10 µM ODQ (**e**, purple horizontal zone, n= 12 arterioles from 7 mice). **(b, d, f)** Comparisons of arteriolar diameters during the 5-minute baseline period and the last 5 minutes of the 30-minute pharmacologic treatments. Note the absence of statistically significant differences after TTX **(b)**, L-NAME **(d)** and ODQ **(f)** applications. Violin plots summarizing the effects of TTX (brown), L-NAME (orange) and ODQ (purple) on the magnitude **(g1**, $H_{(5,51)}$= 13.053, p= 0.01102**),** maximum **(g2**, $H_{(5,51)}$= 14.761, p= 0.00522**)**, onset **(g3**, $H_{(5,51)}$= 11.795, p= 0.01894**),** time to peak **(g4**, $H_{(5,51)}$= 10.957, p= 0.02705**)**, and duration **(g5**, $H_{(5,51)}$= 9.278, p= 0.05452**)** of vasoconstriction induced by 2 Hz photostimulation. Note the stronger vasoconstriction under L-NAME treatment. Data are presented as individual values. Solid and dashed black bars correspond to median and quartile values. * , ** and *** statistically different from control condition 2 Hz Sst-ChR2 (blue) with p<0.05, 0.01 and 0.001, respectively.

.

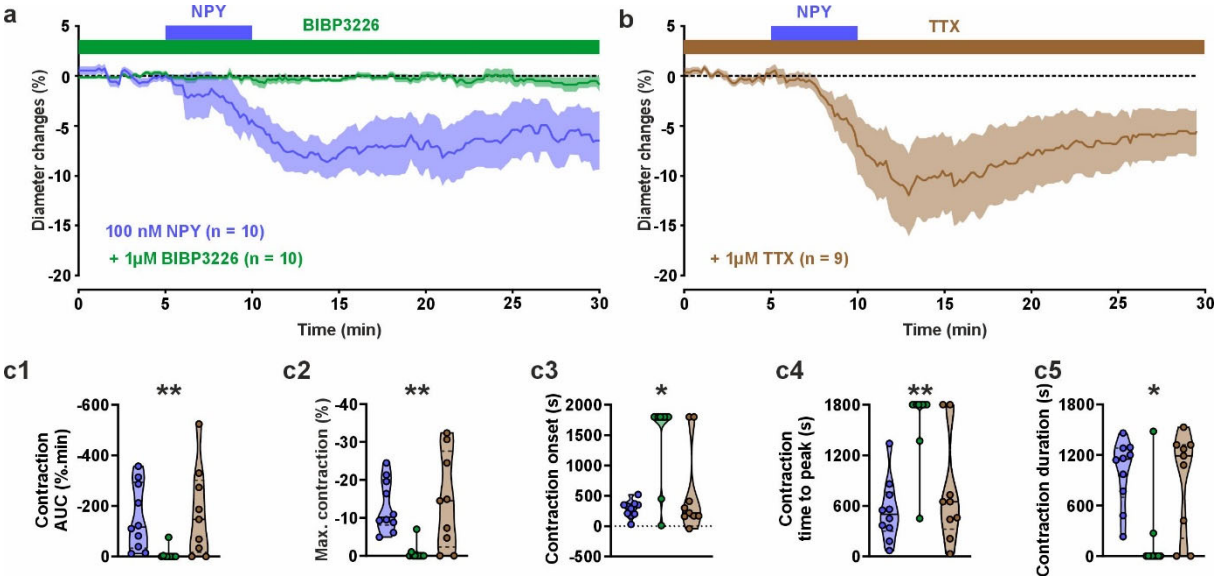

Figure 5: NPY-induced vasoconstriction involves the Y1 receptor independently of spiking activity. (a,b) Kinetics of diameter changes induced by 5 minutes exogenous application of 100 nM NPY (blue bars) under control condition (**a**, blue trace) and in presence of 1 µM BIBP3226 (**a**, green trace, n= 10 arterioles from 6 mice) or 1 µM TTX (**b**, brown trace, n= 9 arterioles from 4 mice). The SEMs envelope the mean traces. Violin plots summarizing the effects of BIBP 3226 (green) and TTX (brown) on the on the magnitude **(c1**, $H_{(4,32)}$= 17.244, p= 0.00063**),** maximum **(c2**, $H_{(4,32)}$= 17.859, p= 0.00047**)**, onset **(c3**, $H_{(4,32)}$= 13.529, p= 0.00362**),** time to peak **(c4**, $H_{(4,32)}$= 16.209, p= 0.00103**)**, and duration **(c5**, $H_{(4,32)}$= 13.557, p= 0.00357**)** of vasoconstriction induced by NPY. The selective NPY Y1 receptor antagonist BIBP3226 but not TTX abolished the NPY-induced vasoconstriction. Data are presented as individual values. Solid and dashed black bars correspond to median and quartile values. * and ** statistically different from the 100 nM control condition with p< 0.05 and 0.01, respectively.

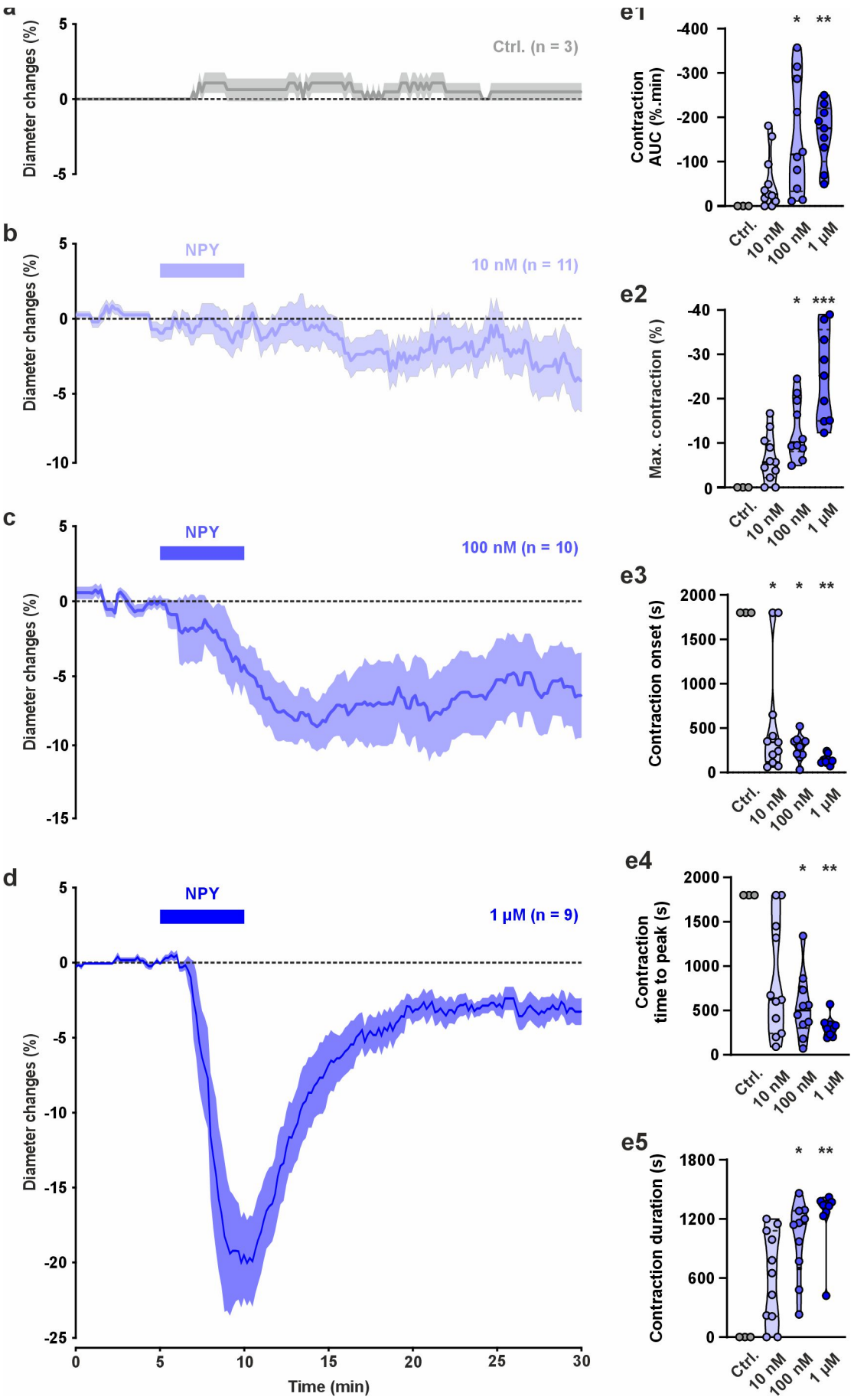
a
Diameter changes (%)
Ctrl. (n = 3)
b
NPY
10 nM (n = 11)
c
NPY
100 nM (n = 10)
d
NPY
1 µM (n = 9)
Time (min)
e1
Contraction AUC (%.min)
e2
Max. contraction (%)
e3
Contraction onset (s)
e4
Contraction time to peak (s)
e5
Contraction duration (s)
Ctrl.
10 nM
100 nM
1 µM

1124

Supplementary Figure 5: The dose-response effects of NPY-induced vasoconstriction. (a-d) Kinetics of diameter changes in absence (**a**, gray, n= 3 arterioles from 3 mice) and in presence of NPY applied for 5 minutes at 10 nM (**b**, light blue, n= 11 arterioles from 7 mice), 100 nM (**c**, medium blue, n= 10 arterioles from 8 mice) and 1 µM (**d**, dark blue, n= 9 arterioles from 4 mice). **(b-d)**. **(e1-3, f1-3).** The SEMs envelope the mean traces. **(e1-5)**. Violin plots summarizing the effects of 10 nM (light blue), 100 nM (medium blue) and 1 µM NPY (dark blue) on the on the magnitude **(e1***,* $H_{(4,33)}$= 14.474, p= 0.00233**),** maximum **(e2***,* $H_{(4,33)}$= 20.060, p= 0.00016**)**, onset **(e3**, $H_{(4,33)}$= 11.740, p= 0.00833**),** time to peak **(e4**, $H_{(4,33)}$= 11.371, p= 0.00988**)**, and duration **(e5**, $H_{(4,33)}$= 17.733, p= 0.00050**)** of vasoconstriction compared to the control condition. Note the lack of consistent diameter changes in the absence of NPY **(a,e)** and the higher magnitude **(e1)** and amplitude **(e2)**, the earlier onset **(e3)** and time to peak **(e4)**, and the longer **(e5)** vasoconstriction with increasing NPY concentrations **(b-d)**. Data are presented as individual values. Solid and dashed black bars correspond to median and quartile values. *, ** and *** statistically different from the control condition with p < 0.05, 0.01 and 0.001, respectively.

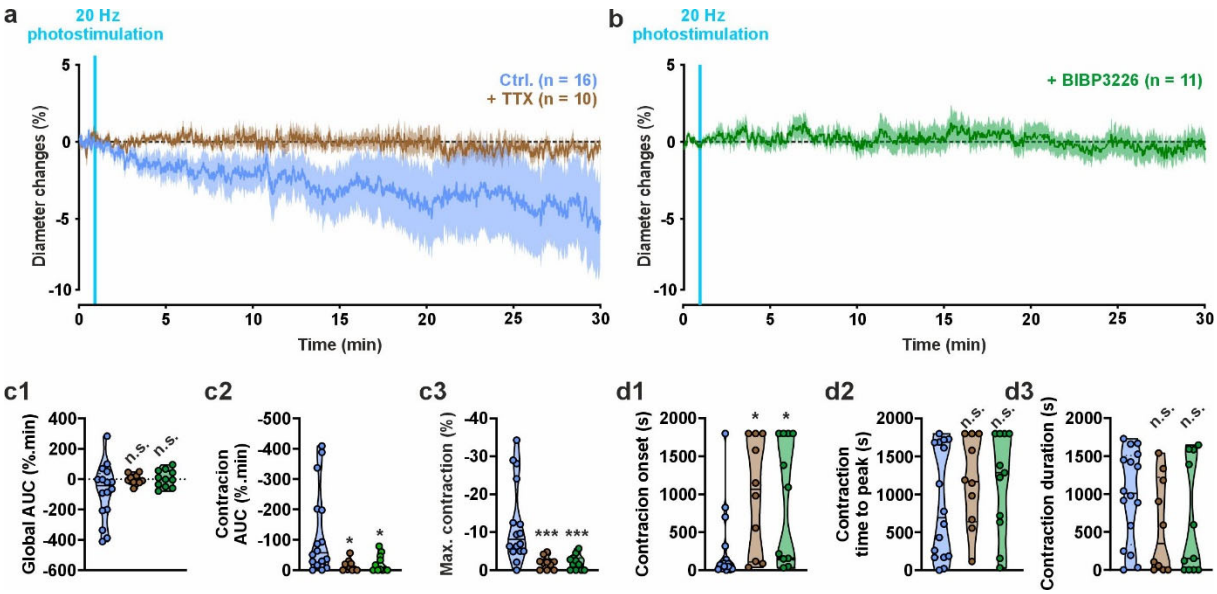

Figure 6: Vasoconstriction induced by 20 Hz photostimulation of Sst-ChR2 neurons requires spiking activity and NPY signaling. (a, b) Effects of tetrodotoxin (TTX, 1 µM, brown, n= 10 arterioles from 5 mice) and the selective Y1 receptor antagonist (BIBP 3226, 1 µM, green, n= 11 arterioles from 9 mice) on the kinetics of the vascular response induced by 20 Hz photostimulation of Sst-ChR2 neurons. The blue trace corresponds to the control condition shown in Fig. 2e. The SEMs envelope the mean traces. Vasoconstriction is abolished by blocking action potentials with TTX **(a)** or by the selective antagonist of Y1 receptor, BIBP 3226 **(b)**. Violin plots summarizing the effects of TTX (brown) and BIBP 3226 (green) on the overall vascular response **(c1***,* $F^*_{(3,22.04)}$= 2.557, p= 0.08117**)**, magnitude **(c2***,* $H_{(4,41)}$= 10.774, p= 0.01301**),** maximum **(c3***,* $H_{(4,41)}$= 19.152, p= 0.00025**)**, onset **(d1***,* $H_{(4,41)}$= 10.671, p= 0.01364**),** time to peak **(d2***,* $H_{(4,41)}$= 6.373, p= 0.09481**)**, and duration **(d3***,* $H_{(4,41)}$= 4.726, p= 0.19300**)** of vasoconstriction induced by 20 Hz photostimulation (cyan). Data are presented as individual values. Solid and dashed black bars correspond to median and quartile values. *, ** and *** statistically different from control condition with p<0.05, p<0,01 and 0.001 respectively.

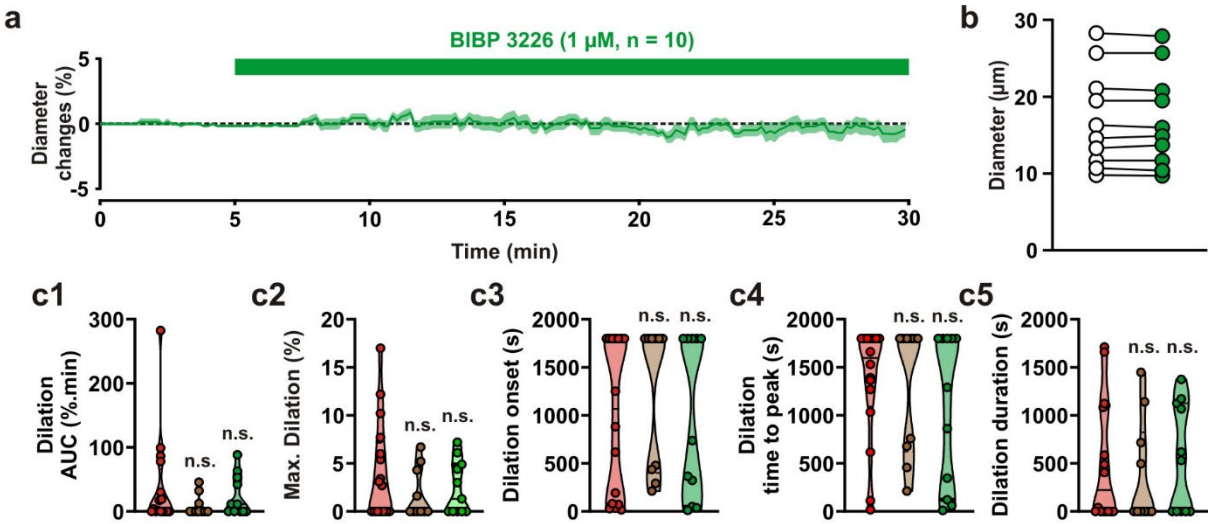

Supplementary Figure 6: Effects of pharmacological treatments on the basal vascular tone and the vasodilation evoked by 20 Hz stimulation. (a) Kinetics of vascular diameter changes during BIBP3226 application. Note the absence of diameter changes during the application of 1 µM BIBP 3226 (**a**, green horizontal zone, n= 11 arterioles from 9 mice). **(b)** Comparisons of arteriolar diameters during the 5-minute baseline period and the last 5 minutes of the 30-minute BIBP3226 treatment. Note the absence of statistically significant differences after BIBP 3226. applications. Violin plots summarizing the effects of TTX (brown) and BIBP3226 (green) on the magnitude **(c1**, $H_{(4,41)}$= 1.947, p= 0.58347**),** maximum **(c2***,* $H_{(4,41)}$= 1.714 , p= 0.63375**)**, onset **(c3***,* $H_{(4,41)}$= 1.401 , p=0.70520 **),** time to peak **(c4***,* $H_{(4,41)}$= 0.815, p= 0.84585**)**, and duration **(c5***,* $H_{(4,41)}$= 0.747 , p= 0.86209**)** of vasodilation induced by 20 Hz photostimulation. Neither TTX or BIBP 3226 alter the vasodilation. Data are presented as individual values. Solid and dashed black bars correspond to median and quartile values. n.s. not statistically different from the control condition 20 Hz Sst-ChR2 control condition (red).

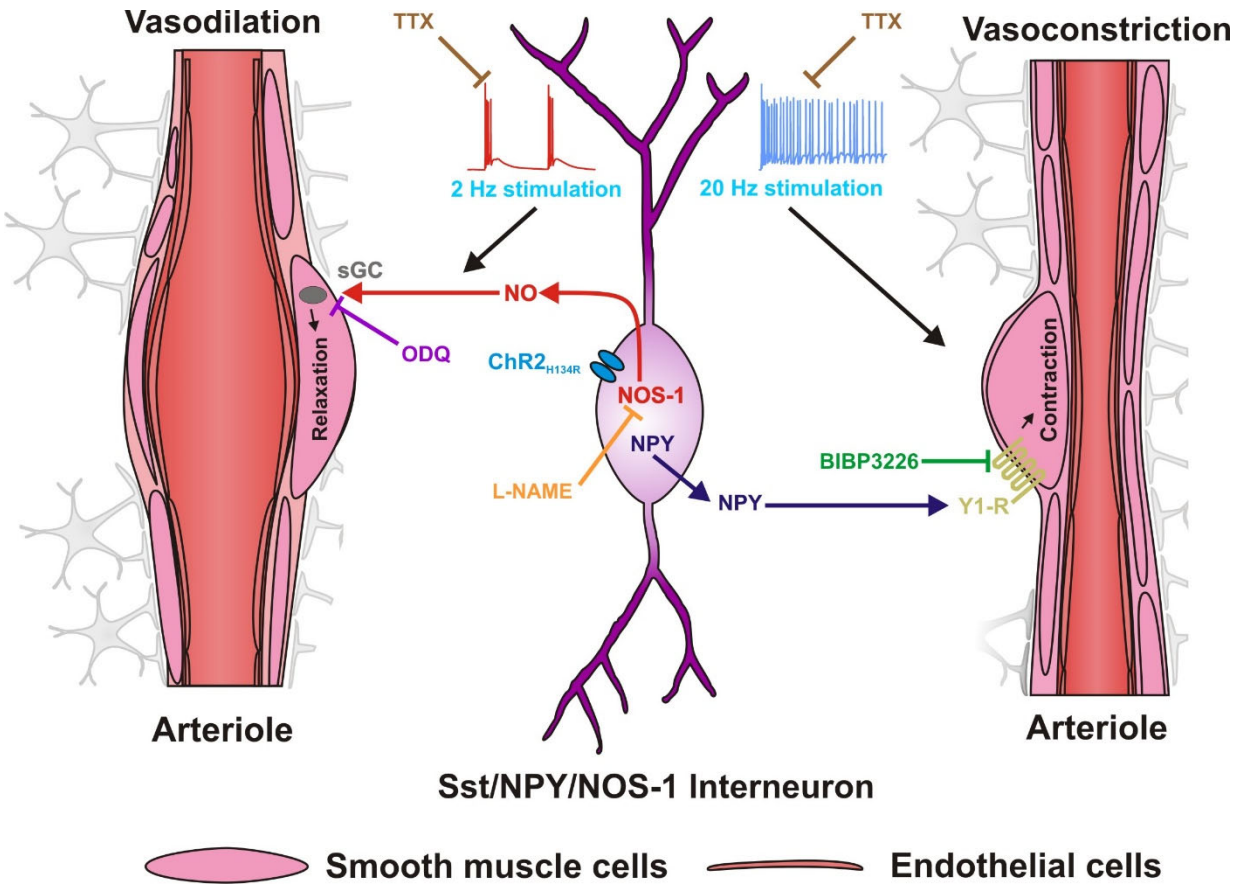

Figure 7: Schematic representation of the mechanisms of bidirectional control of neurovascular coupling by Sst-ChR2 interneurons. Bidirectional responses are shown on both sides of the Sst-NPY-NOS-1 interneuron. **Left:** 2 Hz stimulation of Sst-ChR2 interneurons activates NOS-1 and releases NO which in turn activates the sGC of smooth muscle cells leading to their relaxation and vasodilation. This effect is abolished by TTX (brown) and by inhibition of NOS with L-NAME (orange) and sGC with ODQ (purple). **Right**: 20 Hz photostimulation of Sst-ChR2 interneurons induces NPY release and activation of vascular receptor Y1 leading to smooth muscle cell contraction and vasoconstriction. This effect is suppressed by the TTX (brown) and the Y1 receptor antagonist, BIPB3226 (green).